JOURNAL OF GEOPHYSICAL RESEARCH, VOL. 107, NO. E11, 5110, doi:10.1029/2001JE001614, 2002

Apollo 17 landing site: Topography, photometric corrections, and heterogeneity of the surrounding highland massifs

Mark S. Robinson
Department of Geological Sciences, Northwestern University, Evanston, Illinois, USA

Bradley L. Jolliff
Department of Earth and Planetary Sciences and McDonnell Center for Space Sciences, Washington University, St. Louis, Missouri, USA

Received 7 September 2001; revised 12 December 2001; accepted 26 March 2002; published 23 November 2002.

[1] A high-resolution digital elevation model for the Apollo 17 landing site (20°N, 31°E) and surrounding region is used to correct the photometry of Clementine ultraviolet-visible multispectral data to standard viewing and illumination geometry on a pixel-by-pixel basis. FeO and TiO_2 concentrations were derived from these topographic-photometrically corrected data, and steep-sloped highland massifs are used to assess the magnitude of the effects of the correction. The effects are significant, yielding errors as high as 5 wt% FeO and 4 wt% TiO_2 (absolute) on 30° slopes. The magnitude of the correction varies for Sun-facing versus anti-Sun slopes, with greater changes on anti-Sun slopes. Because most of the Apollo 17 sample stations were on surfaces with low slope values (<5°), the topography has only a small effect on the use of the Apollo 17 site for calibration of FeO and TiO_2 parameters. Topographically corrected data and derived compositional information are used to show accurately the variation in composition of the highland units such as the massifs and the Sculptured Hills on a fine scale. Massif compositions are consistent with mixtures of noritic impact melt and feldspathic granulitic material, plus variable amounts of high-Ti basalt on flanks at low elevations and pyroclastic deposits at high elevations, as surmised from previous studies. An unexpected enrichment in FeO at intermediate elevations in some places where massif surfaces have not been covered by mass wasting of impact-melt rich material signals an older volcanic component not previously recognized. This component may be correlative with an old, high-plains volcanic unit exposed northeast of the landing site and north of the Sculptured Hills. Downslope movement of regolith on steep slopes appears to have resulted in compositional or grain size sorting, leading to an apparent enrichment in FeO and TiO_2 from volcanic glass in valleys and draws. The Sculptured Hills have highly variable compositions, ranging from feldspathic patches to exposures of mafic rocks. A strong but localized mafic anomaly within the Sculptured Hills may be a small, postbasin volcanic feature consisting of very low Ti basalt. *INDEX TERMS:* 5410 Planetology: Solid Surface Planets: Composition; 5464 Planetology: Solid Surface Planets: Remote sensing; 5470 Planetology: Solid Surface Planets: Surface materials and properties; 6250 Planetology: Solar System Objects: Moon (1221); *KEYWORDS:* Clementine, Apollo 17, iron, titanium, Lucey method, Moon

Citation: Robinson, M. S., and B. L. Jolliff, Apollo 17 landing site: Topography, photometric corrections, and heterogeneity of the surrounding highland massifs, *J. Geophys. Res.*, *107*(E11), 5110, doi:10.1029/2001JE001614, 2002.

1. Introduction

[2] The 1994 Clementine mission [*Nozette et al.*, 1994; *McEwen and Robinson*, 1997] acquired a global ultraviolet-visible (UVVIS) multispectral data set for the Moon that enabled a new generation of global compositional and mineralogical information at resolutions as high as ~100–250 m/pixel [*McEwen et al.*, 1994; *Pieters et al.*, 1994]. The UVVIS slope coupled with the ~1 μm ferrous absorption feature provides information on the relative abundance of ferrous minerals and Ti-bearing oxides in the lunar regolith, and using sample-based regolith compositions, UVVIS-derived spectral parameters can be calibrated to absolute abundances [*Lucey et al.*, 1995, 1998a, 2000a, 2000b; *Blewett et al.*, 1997]. The more recent Lunar Prospector (LP) remote-sensing-derived geochemical data sets [*Lawrence et al.*, 1998; *Feldman et al.*, 2000] also provide global coverage, but at a much lower resolution, that is, nominally 2°/pixel (~60 km). The Lunar Prospector gamma-ray spectrometer (LPGRS) obtained data on Fe and Ti concentrations that can be compared directly to values derived from Clementine spectral reflectance (CSR) data

0148-0227/02/2001JE001614$09.00

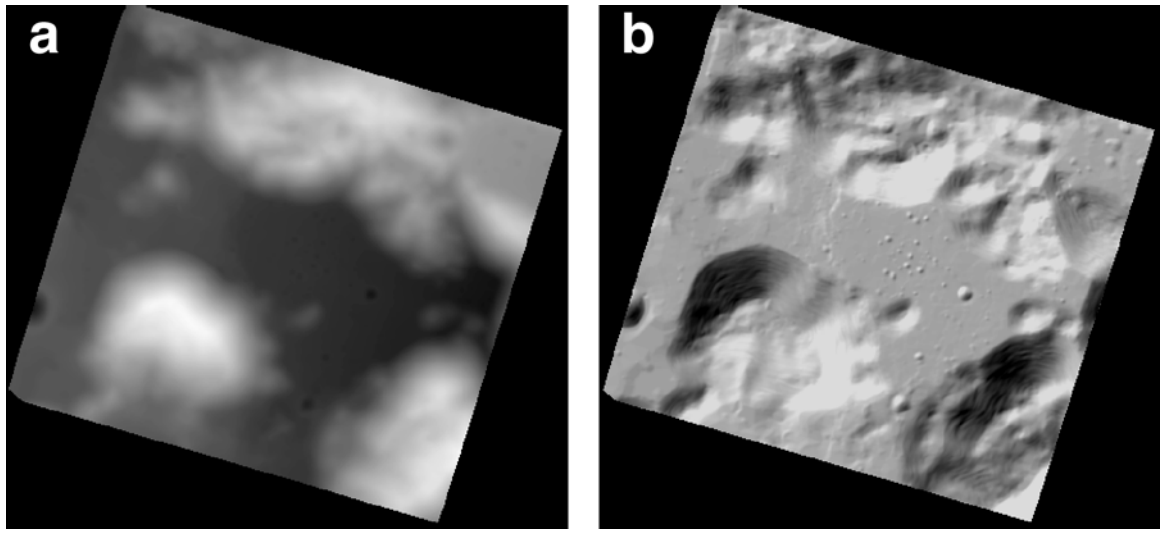

Figure 1. (a) Topographic map digitized from map sheet (USGS unpublished overlay). Original contours were stored at 10 m/pixel and interpolated to continuous digital elevation model (DEM). Data shown here were resampled to 100 m/pixel to match the resolution of the image data (bright values indicate higher elevations, and darker values represent lower elevations; total range of elevations 2–4104 m). (b) Shaded relief map created from the DEM using the same lighting conditions as Clementine frame lub3274l.289 (compare to Figure 3; incidence angle 30°, lighting from SE). Total width of frame is ~45 km; sinusoidal equal area projection; latitude is (19.42°, 20.82°); longitude is (29.88°, 31.47°); north is to the top.

(although data calibration and reduction are still ongoing [*Lawrence et al.*, 2000]). The Lunar Prospector neutron spectrometer (LPNS) obtained data that can also be used to assess Fe and Ti concentrations coupled with other thermal neutron-absorbing elements [*Elphic et al.*, 1998a, 1998b, 2000]. Thus the Clementine and Lunar Prospector data sets can be integrated such that Lunar Prospector data provide accurate measurements over broad areas and the Clementine data provide a means to extend compositional information to high resolution.

[3] Efforts are ongoing to integrate data from the two missions [e.g., *Elphic et al.*, 1998a, 1998b, 2000; *Nozette et al.*, 2001]. Clementine data may be resampled and coregistered with the corresponding LP data for direct comparison at regional scales (2°/pixel). Preliminary efforts at such direct comparisons show good, but not perfect, correspondence [*Gillis et al.*, 2002]. CSR-derived FeO concentrations [*Lucey et al.*, 2000a, 2000b] are based on a parameter that relies on both the 750 nm reflectance and a measure of the ~1 μm absorption, that is, the 950/750 nm ratio. Different ferrous silicates as well as different Fe-bearing volcanic and agglutinatic glasses produce absorptions of different intensity and maximum absorption positions; thus the method is susceptible to variations in, for example, the pyroxene to olivine ratio in soils that may deviate from the typical Apollo and Luna soils used for empirical calibration.

[4] The strength of the CSR empirical calibration is that individual Apollo and Luna sample stations can be resolved in the Clementine data, yielding an empirical calibration that is based on some 48 separate data points [*Blewett et al.*, 1997]. Its weakness is that the parameters used to estimate FeO and TiO_2 concentrations are affected by second-order factors not related directly to FeO and TiO_2. Such factors include mineral and glass types and proportions, variations in proportions of rock and mineral components in different soil grain sizes, level of maturity, and photometric and shading effects related to topography. The latter is especially important in high-resolution studies because the compositional algorithms are strongly dependent on albedo. The calibrations of FeO and TiO_2 developed by Lucey and coworkers [*Lucey et al.*, 1995, 1998a, 1998b, 2000a, 2000b; *Blewett et al.*, 1997] rely on the average compositions primarily of the Apollo soils and are formulated to minimize effects of optical maturity (see especially *Lucey et al.* [1998a, 2000b]). Although *Lucey et al.* [1998a] addressed specifically the uncertainties associated with phase angle and shading variations, no systematic attempt has been made to account for these effects using photometric corrections based on high-resolution digital elevation models.

[5] This paper is concerned specifically with local topographic effects on the derivation of spectral interpretations and on FeO and TiO_2 values derived from Clementine UVVIS color data. Local incidence, emission, and phase angles for each pixel in a Clementine frame are calculated and used in photometric normalization on the basis of the corresponding digital elevation model (Figure 1). Standard photometric processing techniques for the Clementine color data rely on the assumption of a spherical Moon, ignoring local topographic features such as rilles, craters, and basin massifs, which often have slopes exceeding 20°.

[6] The topographic/photometric correction is pertinent to methods of interpretation that rely on reflectance rather than band ratios alone. In this study the Apollo 17 landing site is selected for analysis for several reasons. (1) A very high-resolution stereo topographic map based on Apollo photography exists that has been digitized and the contours interpolated to a shape model (Figure 1). (2) The phase angle is >20° in the corresponding Clementine image data; thus the topographically induced errors in the Lucey method for FeO and TiO_2 were predicted to be significant [*Lucey et*

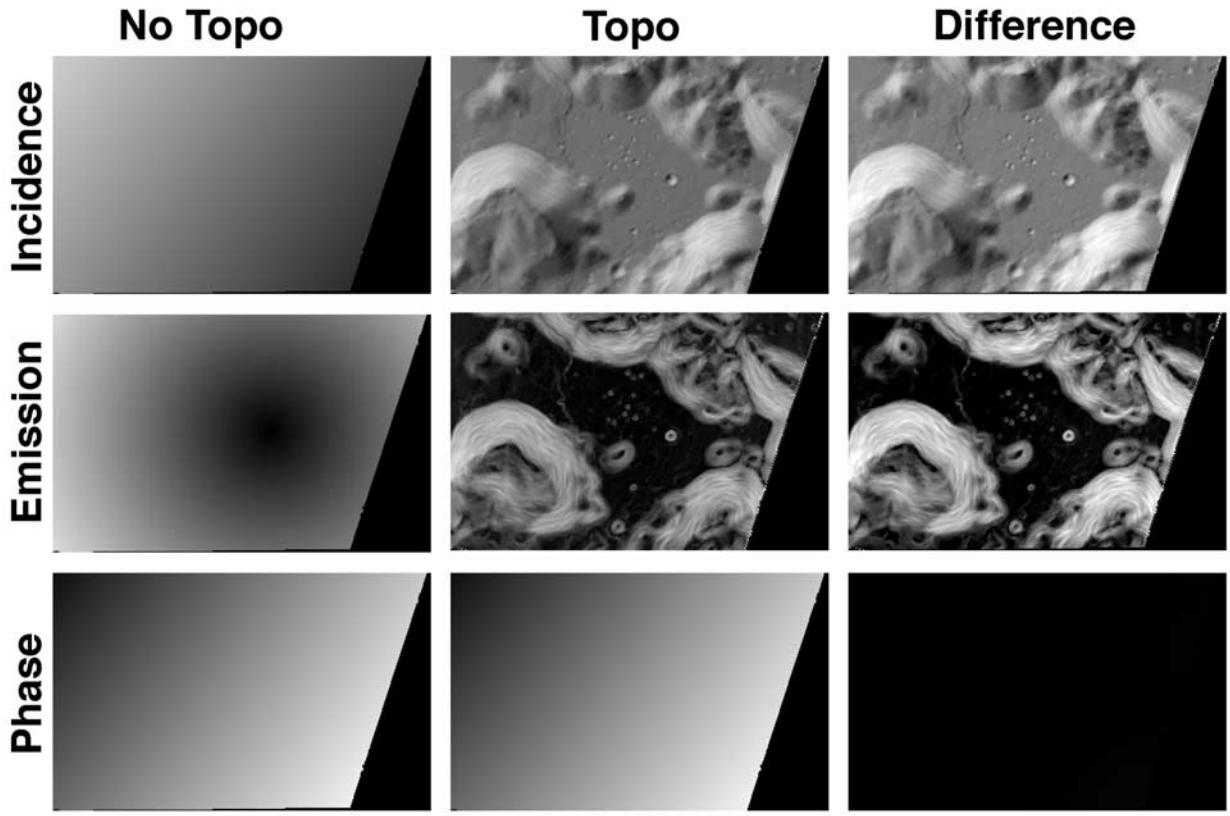

Figure 2. Maps showing incidence angle (top row), emission angle (middle row), and phase angle (bottom row) of the Apollo 17 region shown in Figure 1. The first column shows parameters assuming a spherical planet with no local topography (range: emission 0°–4°, incidence 30°–32°, phase 27°–33°); the second column shows same parameters after accounting for local variations in topography (range: emission 0°–35°, incidence 5°–63°, phase 27°–33°). The third column is a difference image of the first two columns (range: emission −2°–32°, incidence −26° to 32°, phase 0°). Total width of frame is 39 km; north is to the top.

al., 1998a]. (3) Prominent highland massifs surround the landing site with steeply sloping topographic facets (i.e., North Massif and South Massif). (4) Individual sampling stations resolvable in the CSR data have been used in the FeO and TiO_2 empirical calibrations and can be used as comparison sites in the corrected mosaic [*Blewett et al.*, 1997; *Lucey et al.*, 1998a, 2000; *Jolliff*, 1999]. (5) The Taurus-Littrow Valley is known to have deposits of pyroclastically emplaced volcanic materials [*Scott and Carr*, 1972; *Lucchitta*, 1972; *Schmitt*, 1973; *Schmitt and Cernan*, 1973; *Pieters et al.*, 1974; *Wolfe et al.*, 1981; *Gaddis et al.*, 1985; *Hawke et al.*, 1989, 1991], which are mixed into regional soils and may occur in patches on massif slopes that are difficult to detect or which may be spuriously mapped in uncorrected data. (6) A prominent high-albedo feature emanates from the summit of South Massif and extends onto the relatively flat floor of the valley. This feature is proposed to be a landslide or surge deposit caused by secondary impacts from Tycho [*Wolfe et al.*, 1975; *Lucchitta*, 1977; see *Wilhelms*, 1987, Figure 13.11]. Because this feature lies on a steep slope and a valley floor, it is useful to investigate the slope-corrected albedo for both parts of the deposit. Recent studies that have used Clementine data to investigate the Apollo 17 site and surrounding region [*Weitz et al.*, 1998; *Jolliff*, 1999] recognized the effects of topography on Clementine UVVIS photometry but did not attempt to account for them.

2. Method

[7] The topographic data used in this study were digitized from the U.S. Geological Survey (USGS) 1:50,000 scale map of the Taurus-Littrow Valley [*USGS*, 1972] (contours 50 m with 10 m intermediate contours). The digitized contours were interpolated to a continuous gridded digital elevation model (DEM) at a scale of 10 m/pixel (using the TIN module of ARC-INFO©). The DEM was then reprojected to a map scale and projection appropriate for the Clementine image data (Figure 1). To insure proper registration between the Clementine image data and the DEM, match points were selected between a shaded relief map and the Clementine frame (shaded relief was created from the DEM with similar lighting geometry to the Clementine frame lub3274l.289); control points were selected from the centers of four craters on the flat floor of the valley near the center of the Clementine frame to minimize any parallax offsets. The DEM was then translated using these match points with a first-order fit (maximum residual in $x = 0.30$ pixel, maximum residual in $y = 0.45$ pixel). This minor tweak was necessary because of offsets between the Apollo control network and the new

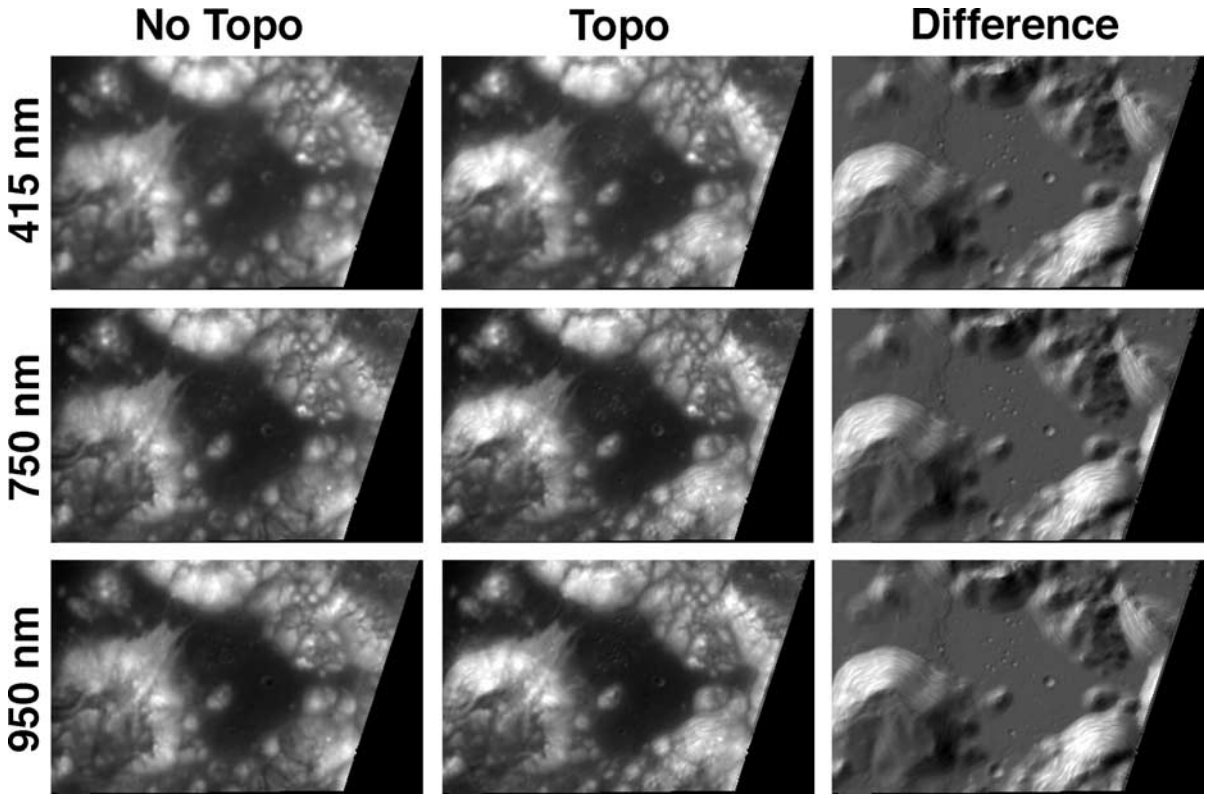

Figure 3. Clementine UVVIS images. The top row shows lua3279l.289 (415 nm), the middle row shows lub3274l.289 (750 nm), and the bottom row shows lud3267l.289 (950 nm). The first column shows photometric correction not using topography, the second column shows photometric correction with topography, and the third column shows difference image topo-notopo (topography corrected image minus uncorrected image).

Clementine global control network [*Lee et al.*, 1997], errors in the map sheet due to geometric instability of the media, and any other unknown geometric discrepancies.

[8] The 415, 900, 950, and 1000 nm filter images were then coregistered (~0.2 pixel accuracy) to the 750 nm frame which was controlled as part of the global control network [*Lee et al.*, 1997]. From the matched DEM, the lunar radius for each pixel in the image was determined, accounting for topographic distortions (parallax), from which an orthorectified five-band image cube was produced. Next the local incidence, emission, and phase angles were calculated for each pixel and stored in image backplanes for later use in the photometric correction (Figure 2). Finally, the wavelength-dependent photometric correction of *McEwen* [1996] and *McEwen et al.* [1998] that was used in the production of the Clementine global map [*Lee et al.*, 1997; *Robinson et al.*, 1999] was applied to the coregistered five-band image set using incidence, emission, and phase angles calculated for each pixel from the topography and the position of the Sun at the time the Clementine images were acquired (Figure 2).

[9] Normalized reflectance values at 415, 750, and 950 nm were used according to methods described previously [*Blewett et al.*, 1997; *Lucey et al.*, 1998a; *Jolliff*, 1999; *Lucey et al.*, 2000a, 2000b] to calculate FeO and TiO_2 concentrations using data resampled to 100 m resolution (angular resolution of a pixel in the original image data ~106 m). Correlation parameters used in these calculations were derived specifically for this data set and are described in section 3.2. Because the 415 nm data have an effective resolution about half that of the other filters (due to differences in point spread function), we use data resampled at 200 m for all quantitative applications of compositional data other than the landing site calibration, for which we compare and discuss different resolutions.

3. Results

3.1. Topography Versus No Topography: Reflectance, Composition, and Maturity Estimates

[10] Fully processed Clementine images at 415, 750, and 950 nm are shown before and after the topographic photometric corrections along with corresponding difference images in Figure 3. In the vicinity of the Apollo 17 landing site, highland massifs rise some 2.5 km above the adjacent basaltic plains, and the massifs commonly have slopes up to 30° that extend over distances of several kilometers. Craters in the area occur within highlands and on the Taurus-Littrow Valley floor and range in size up to about 10 km. Associated with these craters are steep rims and interior slopes. The topographic effects on measured reflectance are shown clearly in the difference images of Figure 3, which essentially mirror topography, but with the strongest effects on slopes facing directly toward or away from the Sun.

[11] Images of derived FeO, TiO_2, and maturity are shown in Figure 4 before topographic correction and after topographic correction; also shown is the difference between the

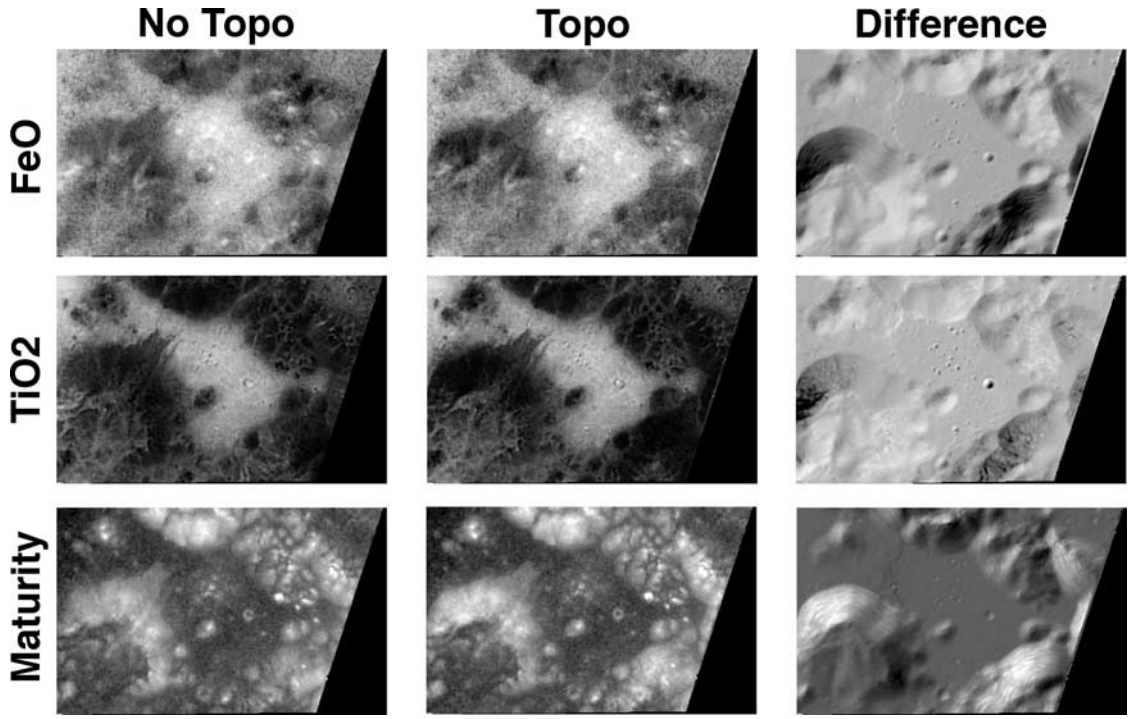

Figure 4. Compositional and maturity images. The top row shows FeO, the middle row shows TiO_2, and the bottom row shows maturity. The first column is without topographic correction, the second column is with topographic correction, and the third column shows the difference map (topography correction minus no topography correction). Same area as shown in Figures 1 and 2; total width of frame is 39 km, north is to the top.

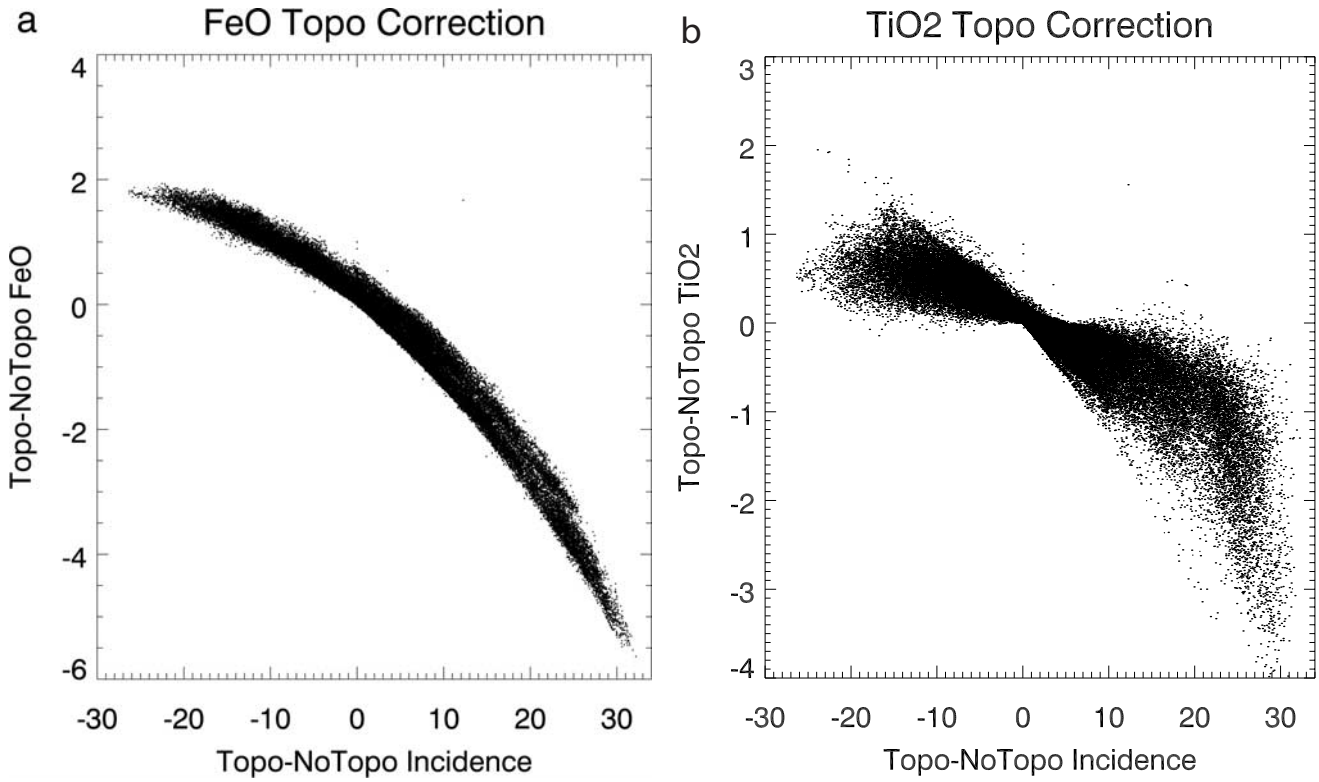

Figure 5. (a) Scatterplot of FeO difference image versus incidence-angle difference image. (b) Scatterplot of TiO_2 difference image versus incidence angle difference image (see also Figures A1 and A2).

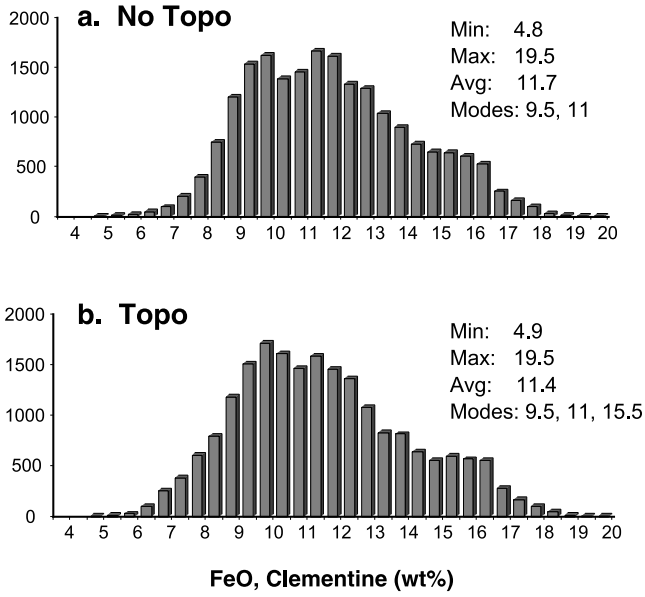

Figure 6. FeO histograms for the Taurus-Littrow region (a) without topographic correction and (b) with topographic correction. These two figures show good agreement, but only because there are compensating errors in the uncorrected data. Histograms are for data resampled to 200 m resolution.

two, which highlights areas of steep slopes. The magnitude of the topographic correction on the derived compositional parameters, summarized in Figure 5, is asymmetrically disposed relative to incidence angle (see additional material in Figures A1 and A2); however, the effects associated with bright, Sun-facing slopes and darker slopes that face away from the Sun tend to cancel each other when averaged over an area greater in scale than the topographic feature in question. Nonetheless, the effects associated with topography cause significant error in quantitative derivations of composition when the scale of investigation is smaller than the topographic features being examined. For example, Figures 6 and 7 show the distribution of derived FeO and TiO_2 concentrations in histograms covering the entire area shown in Figure 4. In this case the histograms of FeO values derived from corrected and uncorrected data are quite similar, as would be the derived FeO and TiO_2 values integrated over large areas, e.g., 5–10 km or greater, in the absence of a significant regional slope. For FeO the means for uncorrected and corrected values for the entire image are 11.7 and 11.4 wt%, respectively. For TiO_2, uncorrected and corrected mean values are 3.1 and 3.0, respectively. Minima, maxima, and modes are also similar (Figures 6 and 7).

[12] For a subsample of the data where slopes are steep, however (e.g., for an area covering the western half of South Massif), the differences in derived FeO and TiO_2 are substantial, with the mean too high by 1% FeO and 0.5% TiO_2 (absolute wt%) in the uncorrected data (Figure 8). More important, the shape of the distribution changes significantly to distinctly bimodal for both FeO and TiO_2. In an extreme case of shading (e.g., on the NW slope of South Massif), the average FeO value changes from 15 wt% before the correction to 11 wt% after the correction, and TiO_2 changes from 4 to 1.5 wt% (Table 1). On the southeastern flank of South Massif in an area of steep Sun-facing slope, the average FeO value changes from 8.7 before correction to 10.1 wt% after correction, and TiO_2 changes from 1.1 to 1.7 wt%. If ignored, these errors could lead to incorrect interpretations of (1) FeO-rich regolith, perhaps associated with pyroclastic deposits, on the western massif slopes and (2) significant differences between massif materials on the western and eastern slopes. As shown in Figure 9, when corrected for topography, compositions of these massif materials are essentially the same except for a small group of FeO-rich pixels on the western (anti-Sun) slope. With the corrected data the major rock types represented by these soil compositions may be interpreted with increased confidence (see section 4.1).

3.2. Calibration of FeO and TiO_2

[13] Although most of the Apollo 17 sample stations were on relatively flat terrain (at the 100 m scale), some were not, notably those that were along the southern slopes of North Massif, such as Stations 6 and 7, and LRV 10 (Figure 10). In this section we present the data for the sample-station soils and examine the FeO and TiO_2 calibrations.

[14] The UVVIS spectral data for the sample stations are given in Tables A1 and A2 for the sample stations and for several representative locations on steep slopes in Table A3. Values of FeO and TiO_2 are derived by the methods described by *Jolliff* [1999] and *Lucey et al.* [2000a, 2000b]. Prior to calculation of FeO and TiO_2 the reflectance data were normalized as described by *Blewett et al.* [1997] and *Jolliff* [1999] using the following factors: A filter, 1.0925; B filter, 1.1704; D filter, 1.1937 (C filter, 1.1574; E filter 1.2098). We used an optimized origin (as defined by

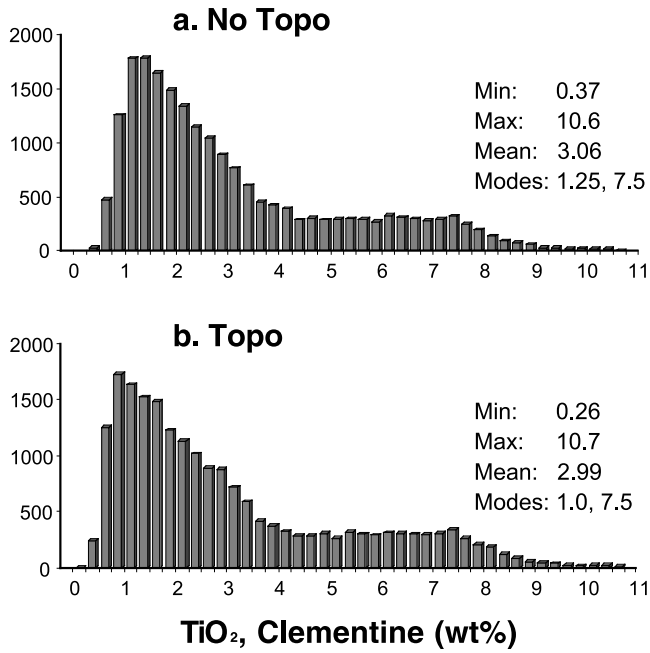

Figure 7. TiO_2 histograms for the Taurus-Littrow region: (a) without topographic correction and (b) with topographic correction. These two figures show good agreement, but only because there are compensating errors in the uncorrected data. Histograms are for data resampled to 200 m resolution.

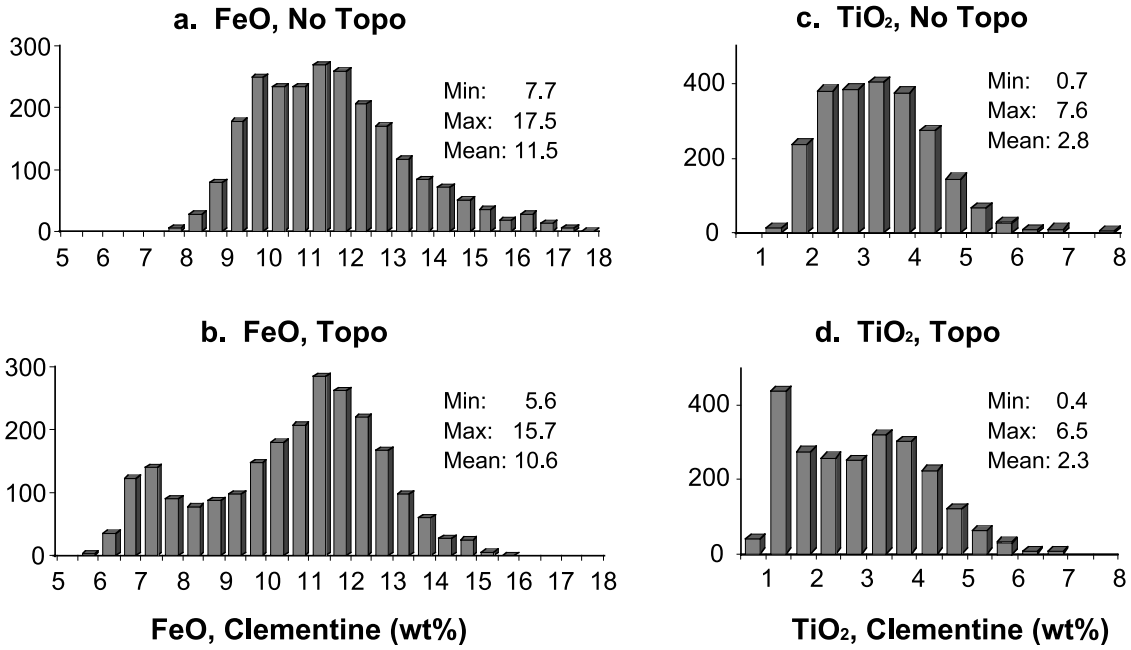

Figure 8. Histograms showing (a and b) FeO and (c and d) TiO_2 distributions before and after topographic correction for a subset of South Massif (western half; latitude longitude range is 19.668° to 30.133° and 20.143° to 30.350°). The main topographic effect on this side of the massif is shading; thus the topographic correction reduces FeO and TiO_2 values on the slopes. For this subarea the shapes of the distributions change from essentially unimodal to distinctly bimodal. Highest values occur at the base of the slopes adjacent to basaltic plains. Data resolution is 200 m per pixel.

Lucey et al. [1995, 1998a, 2000]) at (750 nm = 0.04, 950/750 = 1.22) for FeO and (750 nm = 0.05, 415/750 = 0.45) for TiO_2, and we used the following equations for both the topography-corrected and uncorrected data sets:

$$\theta_{Fe} = -\arctan[(950\text{ nm}/750\text{ nm} - 1.22)/(750\text{ nm} - 0.04)] \quad (1)$$

$$\theta_{Ti} = \arctan[(415\text{ nm}/750\text{ nm} - 0.45)/(750\text{ nm} - 0.05)] \quad (2)$$

$$FeO = 20.22\theta_{Fe} - 3.95 \quad (3)$$

$$TiO_2 = 4.738\theta_{Ti}^{4.298} \quad (4)$$

[15] Figures 11 and 12 compare the results for the sample-station calibration points for FeO and TiO_2, and the values are listed in Tables 2 and 3 (for the sample station analysis in this section we used 100 m/pixel sampling). The fits (comparing Clementine-derived values to measured concentrations [*Morris et al.*, 1983; *Korotev and Kremser*, 1992]) are very similar, as expected, because most of the calibration points (sample stations) are located in relatively flat areas. Only three points have significantly different topographically corrected values: Station 6, Station 7, and LRV 10. All are on the south facing (Sun-facing) southern slope of North Massif, so the effect of the topographic correction is to lower the normalized reflectance, resulting in an increase in the estimate of FeO concentration. For LRV 10 the correction moves the data point closer to the correlation line, but for Stations 6 and 8 it moves them away from the line. Even without the topographic correction, the Station 6 estimate is already high. We note, however, that these two stations are in areas where there is an FeO concentration gradient related to the slope (i.e., mare-non-

Table 1. FeO and TiO_2 of Areas of Extreme Slope on South Massif Before and After Topographic Correction[a]

			FeO		TiO_2		
	Latitude	Longitude	notopo	topo	notopo	topo	Elevation, m
Bright extreme	19.740°–19.833°N	30.519°–30.575°E					
Maximum			10.2	11.5	1.7	2.5	1607
Mean			8.7	10.1	1.1	1.7	944
Minimum			7.6	9.0	0.5	0.7	306
Standard deviation			0.5	0.5	0.2	0.3	309
Shaded extreme	19.945°–20.024°N	30.168°–30.210°E					
Maximum			17.5	13.7	6.3	3.1	1777
Mean			14.8	11.1	3.9	1.5	1256
Minimum			12.3	8.8	2.2	0.7	716
Standard deviation			1.3	1.2	0.9	0.5	258

[a]Elevation is relative to Apollo 17 ALSEP. FeO and TiO_2 are in weight percent; notopo, before topographic correction; topo, after topographic correction.

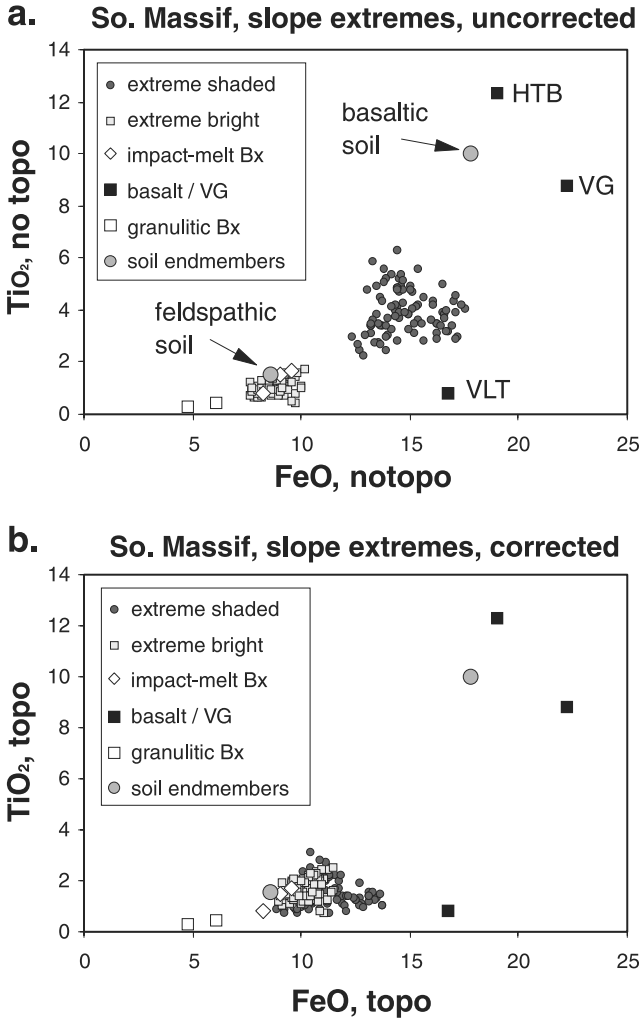

Figure 9. FeO versus TiO_2 concentrations (wt%) of areas of extreme slopes on South Massif (a) uncorrected and (b) corrected for topography, with compositions of prominent Apollo 17 rock types shown for comparison (see Table 4). The areas of South Massif slopes represented here are dominated by impact-melt breccia mixed with some basaltic components. From the uncorrected data one might conclude that the western slopes had a more significant basalt component or a concentration of pyroclastic material (a). In the corrected data plot (b) the data clusters for the two extreme slope regions merge and yield essentially the same compositional range. (Bx = breccia, HTB = high titanium basalt, VG = volcanic glass, VLT = very low titanium basalt.)

mare mixing) and where variations at constant slope are significant. In fact, the pixel corresponding to Station 6 has the highest FeO of its surrounding eight neighbors, and using the 9-pixel (nearest neighbor) average yields a value that is close to the correlation line (Figure 11). Additionally, the exact location of the sampling sites is not necessarily known to the scale of a Clementine pixel, especially stations such as 6 and 7, which are not located by large craters or other prominent landmarks. In any event, these differences do not affect the calibration significantly. In fact, we obtain essentially the same calibration if we use single pixels associated with each sample station or 9-pixel, nearest-neighbor averages (see Tables 2 and 3). The error bars shown in Figures 11 and 12 represent the standard deviations of the central pixel and its eight nearest neighbors. These error bars are small relative to some of the offsets from the correlation lines for both FeO and TiO_2, suggesting other sources of error (more so for TiO_2 than for FeO), including the possibility that the sampled soils and measured soil compositions are not exactly representative of the larger areas corresponding to individual or multiple pixels in the Clementine images.

4. Discussion

[16] Although the FeO and TiO_2 calibrations derived from the Apollo 17 sample stations are not significantly affected by topography, much of the rest of the surrounding area is, particularly in the hills and massifs that rise from the mare plains and in craters of all sizes. Thus, without a topography-corrected data set, interpretations of local geology based on Clementine-derived compositional estimates are limited in regions with significant topography. With the corrected data set, however, we may investigate variations in FeO and TiO_2 with greater confidence, and we can more accurately investigate variations related to elevation and specific highland geologic units. In the following sections we examine variations in composition derived from the topography-corrected Clementine data in light of compositions of the main rock and soil types known from the Apollo 17 samples (Table 4).

4.1. Surface Compositions, Major Rock Types, and Elevations

[17] At the Apollo 17 site, FeO and TiO_2 concentrations correlate to first order with elevation (Figure 13). In general, the Taurus-Littrow Valley floor contains soils developed on Fe- and Ti-rich basalt flows, whereas higher elevations, including the massifs and other hilly terrain, are generally covered by soils derived from Fe- and Ti-poor, feldspathic rock types. Mixing of highland material onto the basaltic

Figure 10. (opposite) (a) Overview image map of Taurus-Littrow Valley. Numbered yellow boxes correspond to spectral sampling areas detailed in text and Table 5, and lowercase single letters indicate locations listed in Table A3. Arrows indicate a few of the locations where dark mantle materials have accumulated in gullies and draws due to downslope movement; the large arrow to the northwest identifies the largest such deposit. The 20.08°N latitude line is shown in black (see Figure 13). The basemap is composed of Apollo 15 Pan Images 9557–9559 scanned from prints and controlled to Clementine control network (SM, South Massif; FM, Family Mountain; NM, North Massif; A 17, Apollo 17 landing site; BM, Bear Mountain; SH, Sculptured Hills; VM, Vitruvius Mons). (b) Blowup of central portion of Figure 10a with overlay of Lunar Rover traverses. Sample stations and LRV stations are indicated with S number and L number, respectively; the location of the lunar module Challenger is indicated with a red dot. Adapted from maps shown by *Wolfe et al.* [1981] and *Muehlberger et al.* [1973].

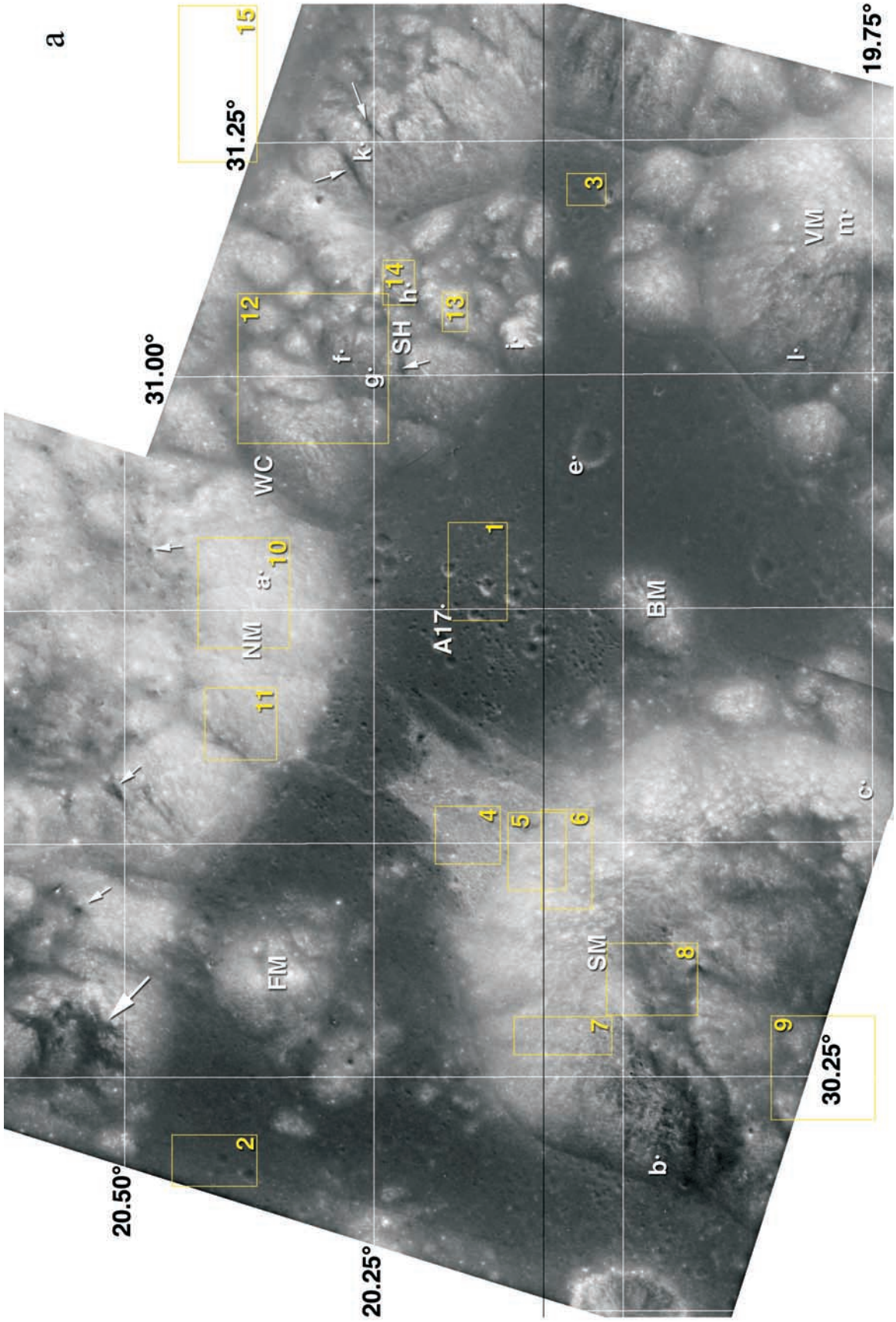
a
31.25°
31.00°
20.50°
20.25°
30.25°
19.75°
WC
NM
FM
SM
BM
A17
SH
VM
1
2
3
4
5
6
7
8
9
10
11
12
13
14
15
a
b
c
e
f
g
h
i
k
l
m

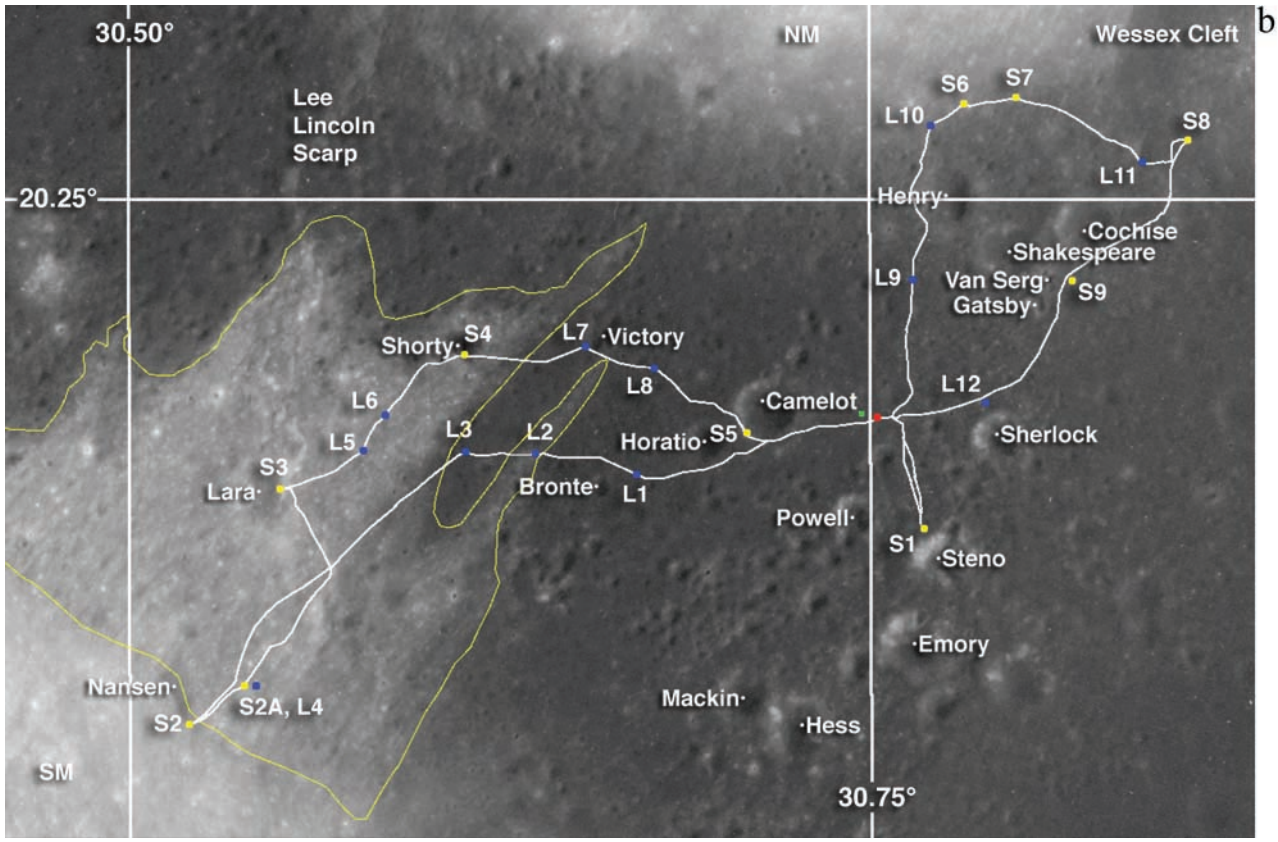

Figure 10. (continued)

valley floor by impact processes and related downslope mass wasting complicates this simple relationship. Basaltic components are also mixed into upslope soils as ejecta from impacts into the valley floor and as ballistically emplaced pyroclastic material. Using the combined topographic and compositional data sets, we can assess these effects as well as variations in the highlands units that might be associated with elevation and thus be related to impact or volcanic stratigraphy.

[18] Analysis of returned samples has allowed the identification of three main groups of lithologies at the Apollo 17 landing site: high-Ti basalts and corresponding volcanic glasses (FeO 19–22 wt%, TiO_2 8–12 wt%), impact-melt breccia (FeO 8–10 wt%, TiO_2 1–2 wt%), and feldspathic granulite and granulitic breccia (FeO 4–7 wt%, TiO_2: <1 wt%) (Table 4) [*Korotev and Kremser*, 1992; *Ryder*, 1993; *Neal and Taylor*, 1993a, 1993b; *Meyer*, 1994; *Jolliff et al.*, 1996]. Igneous rock types such as norite and troctolite/troctolitic anorthosite are, for these two elements, similar to the impact-melt breccias and the feldspathic granulites, respectively. In terms of FeO and TiO_2, the basalts and the feldspathic granulitic rocks form the end-members, but Clementine-derived, 100 m pixel compositions rarely obtain the end-member rock compositions or even the most extreme soil compositions from among the Apollo 17 samples. Compositional data for the area of the light mantle (Figure 14) that extends onto the valley floor from the northern slope of South Massif illustrates this point and shows that the compositions of the known major rock types encompass the data array as expected if these are the major components of the light-mantle soils. These compositions extend almost exactly from the granulitic lithologies toward the high-Ti basalts and orange volcanic glasses but fall short of the basaltic end-members. Even the most basalt-rich of the Apollo 17 returned soils, however, have significant admixed nonmare components [*Korotev and Kremser*, 1992]. Clementine-derived values only attain such high FeO and TiO_2 values in the ejecta of fresh craters such as on the central valley floor [*Jolliff*, 1999].

4.2. Mare Basalt and Volcanic Glass

[19] Clementine-derived compositions of basaltic soils in the central valley, as exemplified by soils at the landing site, are bounded by the compositions of high-Ti basalt, orange volcanic glass, very low Ti (VLT) basalt, and impact-melt and granulitic breccias, and the compositional cluster lies close to that of the most basaltic central valley soil collected from the Apollo 17 mission (Figure 15). The central valley soil compositions reflect the fact that they are all mixtures of mare basalt and volcanic glass plus proportions of nonmare components ranging from 15 to ~40% [*Korotev and Kremser*, 1992]. Compositions are offset slightly in the direction of VLT basalt, consistent with the small VLT component included in the mixing model of *Korotev and Kremser* [1992]. The composition of orange volcanic glass is shown in Figure 15; however, this glass component does not contribute to the FeO content determined from Clementine spectral reflectance, as discussed below.

[20] Soils developed on basaltic plains in the northwestern corner of the study area are closer to the likely source of the Apollo 17 regional pyroclastic deposit than are the central valley soils. This deposit is at least partly composed of

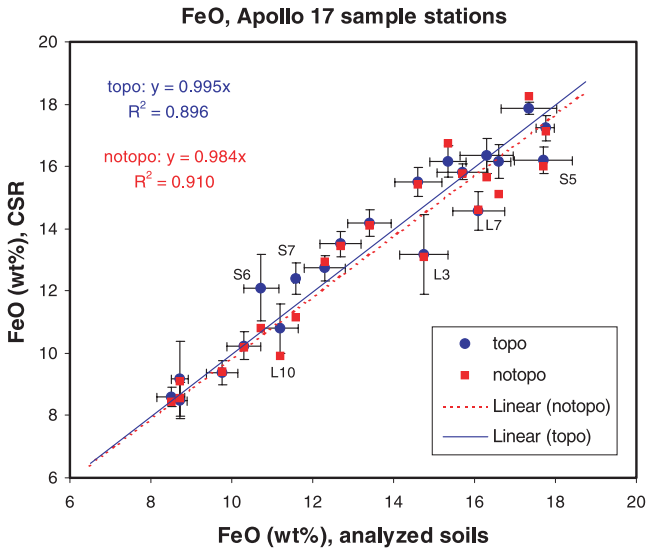

Figure 11. FeO calibration before and after topographic correction. Error bars (shown only for topo-corrected data points) for analyzed soil concentrations are equal to ±1 standard deviation for different analyzed soils collected at each of the stations; these range from 1 to 4% relative standard deviation. For LRV soils, for which there is typically only one soil measurement, error bars for measured FeO are set at ±4%. Error bars for CSR-derived FeO are ±1 standard deviation for the derived FeO values of the center pixel and its nearest eight neighbors. The slope of the regression line for the topographically corrected data is closer to one, but the two regression lines and the R^2 values are not significantly different.

ilmenite-rich black volcanic beads [*Weitz et al.*, 1998], perhaps more so near the source vent than in the soils at the landing site. One potential local source is a volcanic cinder cone observed in the smaller massifs west of the South Massif light mantle slide deposit [see *Wolfe et al.*, 1981, Figure 4]; however, it is generally believed that pyroclastic glasses were most likely erupted from linear fissure vents [*Head and Wilson*, 1992, and references therein]. Orange glass has a low 415/750 value (steep UVVIS slope) for its high Ti content and a low 750/950 value for its high FeO content [*Pieters*, 1993]; thus soils that are richer in orange glass than the central valley soils, where the calibration was done, will have spuriously low CSR-derived FeO and TiO_2. The black beads, which are compositionally equivalent to the orange glass, are ilmenite-olivine vitrophyres in which fine-grained ilmenite coats olivine and gives the beads their black color (summarized by *Wolfe et al.* [1981]). The spectral effect of black volcanic beads is to darken the soils and diminish the UVVIS slope, consistent with their rich ilmenite content, while drastically reducing contrast at the 1-micron absorption [*Pieters*, 1993, Figure 14.9]. Thus CSR-derived FeO concentrations for soils rich in black volcanic beads are decreased (erroneously) relative to the central valley soils (Figure 15). According to the data of *Heiken and McKay* [1974], the central valley soils contain <20% volcanic glass (orange and black), and most contain less than ~7%, except for the glass-rich soil horizons at Station 4 (summarized by *Jolliff* [1999]). The compositions of the soils northwest of the Taurus-Littrow Valley reflect a strong enrichment in volcanic glass, particularly of the black variety. Presumably, black beads characterized later eruptions, thus forming the uppermost layer of volcanic deposits at this site.

[21] Plots of elevation versus FeO and TiO_2 highlight the different areas and compositions of basaltic soils in the Taurus-Littrow region (Figure 13). At the elevation level of the Apollo 17 ALSEP, FeO concentrations reach 19.5 wt%, and TiO_2 reaches 9.2 wt% (Table 5). Compositions of soils in the northwestern area, west of North Massif, at about 250–280 m elevation relative to the ALSEP, form a spike in FeO to about 16 wt%, but corresponding TiO_2 concentrations form a spike reaching nearly 11 wt% (Table 5, Figure 10). This combination of FeO and TiO_2 does not correspond to any of the Apollo 17 basalt types and is too rich in TiO_2 for the relatively low FeO to result from significant nonmare contamination; thus, as indicated above, we interpret this composition to result (erroneously) from high proportions of volcanic glass, especially the ilmenite-rich black variety. Indeed, the FeO concentration of orange and black beads found in the Apollo 17 soils and measured in the laboratory are exceptionally high (i.e., 22 wt% (comparison by *Wolfe et al.* [1981])). Thus, although the measured composition of orange volcanic glass plots at high FeO concentration in Figure 15, Clementine-derived FeO values do not exceed 20 wt% for any of the soils in the study area.

[22] Basaltic soils of the easternmost extents of the Taurus-Littrow Valley (longitude 31.2°, latitude 20.04°) are represented in Figure 13c by a minor spike at the lowest elevations. Presumably, basaltic flows funneled through the entrance to the Taurus-Littrow Valley from a source to the

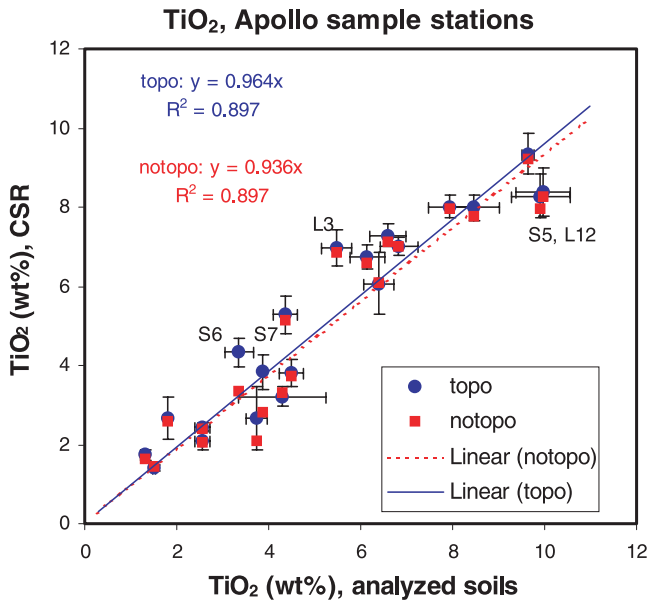

Figure 12. TiO_2 calibration before and after topographic correction. Error bars were determined as for FeO (Figure 11). Tight error bars on measured TiO_2 reflect the typically small variation in measured TiO_2 of sampled soils and do not necessarily reflect accurately the TiO_2 of an entire 0.1 km × 0.1 km area. That the standard deviations of CSR-TiO_2 values for each 3 × 3 box of data centered on a station do not all intersect the regression line, however, suggests that deviation from the line is not due simply to locational errors.

Table 2. Apollo 17 Sample Station Data, FeO[a]

			Measured FeO, wt%	1 Pixel × 1 Pixel		3 × 3	3 × 3 stdev	5 × 5	5 × 5 stdev	Deviation, % Relative	
				topo	notopo	topo	topo	topo	topo	topo	notopo
Station	Latitude, °N	Longitude, °E	(1)	(2)	(3)	(4)	(5)	(6)	(7)	(8)	(9)
LM	20.199	30.742	16.6	15.3	15.1	16.1	0.55	16.3	0.47	8.1	9.0
S1	20.157	30.754	17.8	17.3	17.1	17.5	0.40	17.7	0.59	2.8	3.4
S2	20.099	30.496	8.7	8.5	8.6	8.9	0.59	8.9	0.64	2.9	1.8
S3	20.172	30.534	8.7	9.2	9.1	9.4	1.20	9.6	1.19	5.0	4.5
S5	20.183	30.693	17.7	16.1	16.0	16.2	0.43	16.5	0.68	8.8	9.6
S6	20.289	30.771	10.7	13.8	11.2	12.3	1.06	12.1	1.04	28.6	4.5
S7	20.293	30.785	11.6	12.4	11.2	12.5	0.51	12.3	0.90	7.0	3.6
S8	20.278	30.848	12.3	12.7	12.9	12.6	0.42	12.5	0.85	3.4	5.2
S9	20.227	30.802	15.4	16.8	16.8	16.2	0.52	15.9	0.90	9.2	9.2
L1	20.178	30.655	16.3	15.7	15.7	16.3	0.55	16.1	0.44	3.6	3.9
L2	20.181	30.612	13.4	14.2	14.1	14.3	0.43	14.1	0.54	5.6	5.3
L3	20.181	30.596	14.8	13.1	13.1	13.2	1.28	12.8	1.51	11.1	11.3
L4	20.107	30.517	8.5	8.6	8.5	8.8	0.30	9.2	0.47	0.9	0.5
L5	20.184	30.557	9.8	9.4	9.4	9.5	0.39	10.0	0.69	3.9	3.3
L6	20.194	30.563	10.3	10.2	10.2	9.8	0.45	10.0	0.47	0.6	1.0
L7	20.213	30.634	16.1	14.5	14.6	14.6	0.62	14.1	0.84	9.7	9.2
L8	20.203	30.662	15.7	15.8	15.8	15.8	0.27	15.7	0.61	0.7	0.4
L9	20.233	30.750	14.6	15.5	15.4	15.2	0.47	15.2	0.72	5.9	5.6
L10	20.283	30.753	11.2	10.8	9.9	10.5	0.79	11.0	1.27	3.7	11.3
L11	20.276	30.841	12.7	13.5	13.5	13.5	0.40	13.2	0.53	6.1	6.0
L12	20.197	30.781	17.4	18.3	18.2	17.9	0.19	17.7	0.35	5.8	5.1
										6.3	**5.4**

[a] S indicates station; L indicates LRV stop. Station 4 is not included because the sampled soil is not representative of the local surface [see *Jolliff*, 1999]. Column 1 lists the average soil FeO concentrations as compiled by *Jolliff* [1999]. Topo (column 2) and notopo (column 3) were calculated using the optimized origin of *Lucey et al.* [1998a, 1998b], but regression parameters were determined specifically for this data set (see text). Columns 4 and 6 are 3 × 3 and 5 × 5 pixel averages, respectively, and columns 5 and 7 are the corresponding standard deviations for topographically corrected data centered on single pixels listed in column 2. Columns 8 and 9 show the deviation of the FeO values calculated using the UVVIS data from the measured values (columns 2 and 3), expressed as the percent relative deviation; the average is given at the base of each of these columns. The mismatch for Station 6 accounts for most of the difference between the mean deviations for the corrected and uncorrected data.

Table 3. Apollo 17 Sample Station Data, TiO_2[a]

			Measured TiO_2, wt%	1 Pixel × 1 Pixel		3 × 3	3 × 3 stdev	5 × 5	5 × 5 stdev	Deviation, % Relative	
				topo	notopo	topo	topo	topo	topo	topo	notopo
Station	Latitude, °N	Longitude, °E	(1)	(2)	(3)	(4)	(5)	(6)	(7)	(8)	(9)
LM	20.199	30.742	8.5	8.0	7.8	7.9	0.5	7.8	0.4	5.8	8.2
S1	20.157	30.754	9.6	9.3	9.2	8.8	0.6	8.3	1.2	3.0	4.2
S2	20.099	30.496	1.5	1.4	1.5	1.5	0.1	1.5	0.2	5.5	3.0
S3	20.172	30.534	1.8	2.7	2.6	2.6	0.7	2.3	0.6	47.9	43.5
S5	20.183	30.693	9.9	8.3	8.0	8.2	0.6	8.0	0.8	16.4	19.7
S6	20.289	30.771	3.4	4.3	3.4	4.4	0.4	4.2	0.7	29.3	0.3
S7	20.293	30.785	3.9	3.8	2.8	4.0	0.4	4.0	0.8	1.2	27.2
S8	20.278	30.848	4.3	3.2	3.3	3.2	0.3	3.2	0.4	25.2	22.8
S9	20.227	30.802	6.4	6.1	6.1	6.3	1.1	6.4	1.0	5.0	4.9
L1	20.178	30.655	8.0	8.0	8.0	7.5	0.5	7.6	0.5	0.7	0.2
L2	20.181	30.612	4.4	5.3	5.2	5.3	0.5	5.5	0.9	20.8	18.1
L3	20.181	30.596	5.5	7.0	6.8	6.9	0.7	6.2	1.2	27.0	24.6
L4	20.107	30.517	1.3	1.7	1.7	1.7	0.1	1.5	0.2	34.3	27.2
L5	20.184	30.557	2.6	2.4	2.4	2.4	0.2	2.3	0.2	4.6	5.5
L6	20.194	30.563	2.6	2.1	2.1	2.3	0.3	2.4	0.3	17.6	19.1
L7	20.213	30.634	6.8	7.0	7.0	6.6	0.3	6.5	0.4	2.5	2.5
L8	20.203	30.662	6.6	7.3	7.1	7.2	0.5	7.1	0.7	10.8	8.4
L9	20.233	30.750	6.1	6.7	6.6	6.6	0.3	6.6	0.5	9.7	7.2
L10	20.283	30.753	3.7	2.7	2.1	3.4	0.8	3.5	0.7	28.7	44.1
L11	20.276	30.841	4.5	3.8	3.7	3.8	0.3	3.7	0.5	15.5	17.1
L12	20.197	30.781	10.0	8.4	8.3	8.2	0.7	7.8	0.9	16.0	17.1
										15.6	**15.5**

[a] S indicates station; L indicates LRV stop. Station 4 is not included because the sampled soil is not representative of the local surface [see *Jolliff*, 1999]. Column 1 lists the average soil TiO_2 concentrations as compiled by *Jolliff* [1999]. Topo (column 2) and notopo (column 3) were calculated using the optimized origin of *Lucey et al.* [1998a, 1998b], but regression parameters were determined specifically for this data set (see text). Columns 4 and 6 are 3 × 3 and 5 × 5 pixel averages, respectively, and columns 5 and 7 are the corresponding standard deviations for topographically corrected data centered on single pixels listed in column 2. Columns 8 and 9 show the deviation of the TiO_2 values calculated using the UVVIS data from the measured values (columns 2 and 3), expressed as the percent relative deviation; the average is given at the base of each of these columns.

Table 4. Average Concentrations of FeO and TiO_2 in Common Apollo 17 Materials[a]

Rock/Soil Type	FeO, wt%	TiO_2, wt%	Notes
Poikilitic impact-melt breccia	9.0	1.50	
Aphanitic impact-melt breccia	8.2	0.78	
ITE-rich impact-melt breccia	9.5	1.67	*Jolliff et al.*, 1996
Very low Ti (VLT) basalt	16.7	0.83	
High-Ti basalt	19.0	12.3	
Orange (and black) volcanic glass	22.3	8.8	74220
Ferroan granulitic breccia	6.0	0.45	
Magnesian granulitic breccia	4.8	0.27	
FeO-rich regolith	17.8	10.0	Stations 1, 5
FeO-poor regolith	8.6	1.53	Stations 2, 3

[a] All average compositions from *Korotev* [1998]. ITE, incompatible trace element.

northwest, and the "choke point" between North Massif and South Massif (and Family Mountain) prevented filling of the valley to a uniform elevation. In the eastern valley region, FeO concentrations reach about 17 wt% but average only 15 wt%, and corresponding TiO_2 concentrations reach only about 5 wt%, averaging 4% (Figure 15, Table 5). These basaltic soils are mixed more extensively with nonmare material from the surrounding highland materials, producing soils of intermediate TiO_2 and FeO. Figure 15, however, shows a distinct offset toward high Fe and low Ti, suggesting a nearby source of low-Ti basalt. Alternatively, an early massive (intermediate- to low-Ti) flow from Serenitatis may have inundated the eastern reaches of the valley and may now be covered in the west and central portions of the valley by younger (high-Ti) flows.

[23] Other spikes to relatively high FeO and/or TiO_2 concentrations occur at elevations well above the valley floor (Figure 13). These include an area of relatively high-elevation plains, lying some 1100–1200 m higher than the central valley floor (unit 15, Table 5), and an anomalously high FeO area within the Sculptured Hills at an elevation about 1 km above the central valley floor (unit 14, Table 5). These two areas are discussed in the following sections. Higher still, on both North and South Massifs, soils occur in patches that have FeO and TiO_2 as high as 12 wt% and 3.5 wt%, respectively. These concentrations are too high for any nonmare rock types known from the Apollo samples and may therefore represent local concentrations of volcanic glass in the soils where the pyroclastic materials have not been extensively mixed into and diluted by underlying highland materials as a result of small impact craters. However, the latter unit is on the slopes of the Sculptured Hills, possibly arguing against an origin as pyroclastic blanket material; elsewhere in the region, pyroclastic material appears to move downslope and settle in valleys or depressions. If so, then the material may be a compositional anomaly within the Sculptured Hills.

4.3. Highland Massifs

[24] One of the key problems that can be addressed in the Apollo 17 region is the origin of the different highland units and their relationships to basin-forming events. Prominent massifs rise some 1.5–2.2 km above the basaltic plains and include the North and South Massifs, which were sampled by the Apollo 17 mission, as well as others such as West Massif and Mons Vitruvius (Figures 16 and 17) [*Lucchitta*, 1972; *Scott and Carr*, 1972; *Reed and Wolfe*, 1975; *Wolfe and Reed*, 1976; *Wolfe et al.*, 1981]. These structures are most likely related to faulting and readjustment of crustal blocks following the Serenitatis basin-forming event [e.g., *Reed and Wolfe*, 1975; *Wolfe et al.*, 1981; *Spudis*, 1993].

[25] The massifs appear to be composed of two main groups of nonmare rock components: impact-melt breccias and feldspathic granulitic rocks. The most prominent group of impact-melt breccias are those that have poikilitic texture [*Spudis and Ryder*, 1981]. These breccias occur in the form of large boulders as well as smaller rocks and rock fragments in the soils. Some of the boulders can be shown by prominent and well-preserved tracks to have derived from deposits or exposures higher up on the massif slopes (summarized by *Wolfe et al.* [1981]). It has been suggested that these impact-melt breccias formed by energetic overflow of Serenitatis basin impact melt [*Spudis*, 1993; *Spudis and Ryder*, 1981], although the fabric of the massifs indicates a thick, chaotic, massive ejecta deposit containing melt breccia in discontinuous lenses and pods emplaced simultaneously with fragmented cataclastic debris [*Reed and Wolfe*, 1975]. Key questions surround the detailed distribution of materials within the massifs; for example, where, on or within the massifs, are the impact-melt deposits concentrated? Do they occur at a particular stratigraphic level, and do they lie flat, or do they form irregular lenses within older, more feldspathic prebasin material? Are they concentrated at high elevations on the massifs [e.g., *Jolliff et al.*, 1996]? Do they contain remnants of pre-Serenitatis mare basaltic units?

[26] These questions may be addressed with compositional maps, and here, topographic corrections are important because steep slopes provide access to stratigraphic layering if it is present. The compositional images (Figures 4 and 16) reveal a patch-like distribution of soils rich in impact-melt breccia versus more feldspathic material on the highland massifs, but there appear to be no simple relationships between compositions and elevation (Figure 13). Composition-elevation profiles across the massifs show compositional zones of varying lateral extent, some several kilometers or more across (Figures 18 and 19). In many cases, however, areas of low FeO appear to have been excavated by impacts and distributed onto surrounding surfaces. In areas where feldspathic material is exposed, its FeO and TiO_2 composition lies exactly between that of Apollo 17 impact-melt breccia and granulitic breccias (Figure 20, Table 5). This distribution is consistent with an enrichment of impact-melt breccia in the upper parts of the massifs, underlain by more feldspathic prebasin material. The impacts that created the South Massif light-mantle deposit, presumably Tycho secondaries [*Lucchitta*, 1972], sent landslide or surge-deposit material downslope that was rich in impact-melt breccia (Figure 14). Photographs taken by the astronauts from the landing site show what may be ledges high up on massif slopes (especially North Massif); however, consistent layering is difficult to discern in the Hasselblad 70 mm photographs, and there are no prominent breaks in massif slopes that would indicate specific coherent impact-melt horizons. Thus the upper parts of the massifs appear to be a complex mixture of impact-melt deposits and older feldspathic substrate into which the impact melt was emplaced.

[27] Regoliths developed on melt-rock-rich surfaces of South Massif have FeO and TiO_2 concentrations similar to

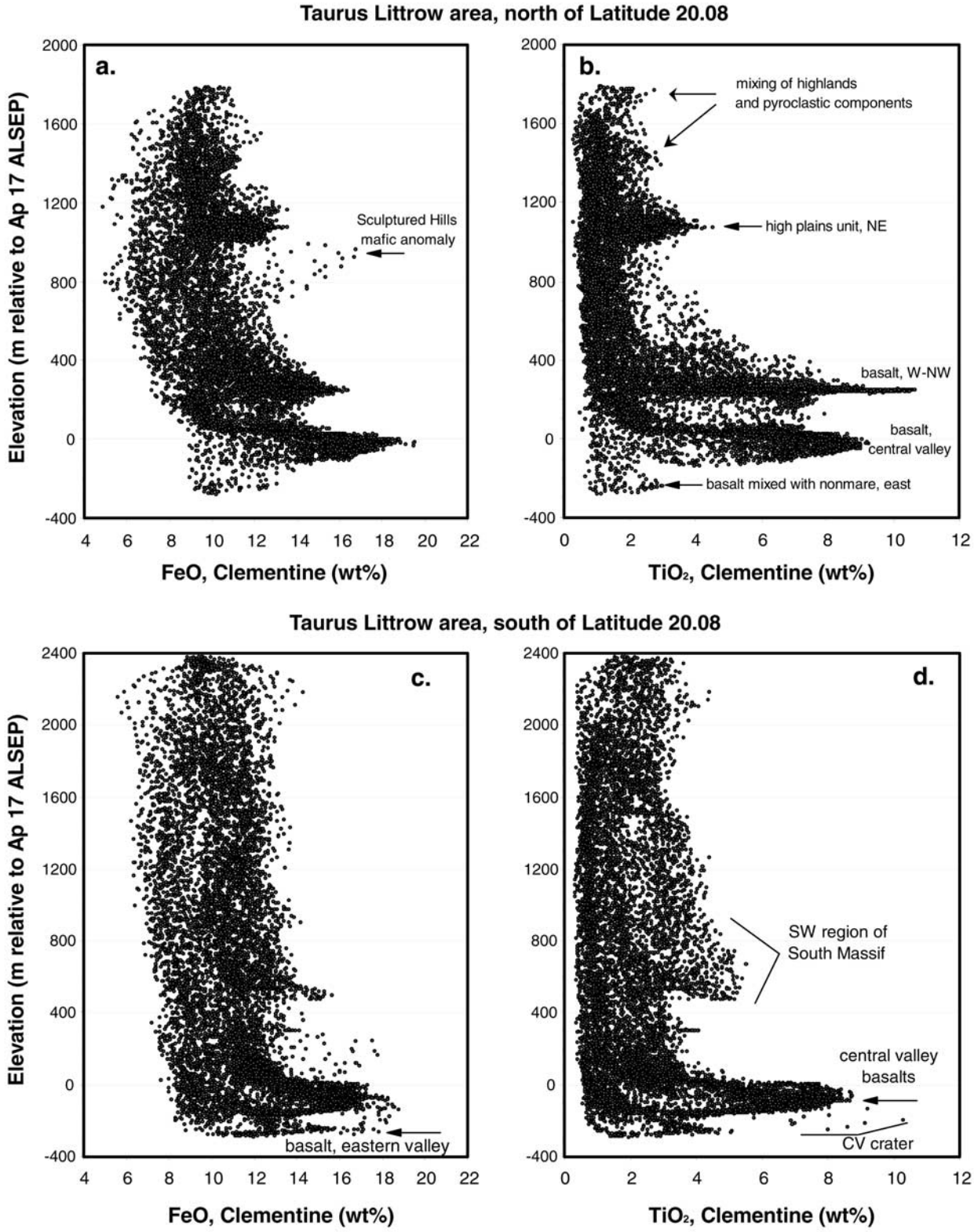

Figure 13. FeO and TiO_2 corrected for topography versus elevation (relative to ALSEP). Compositions were derived from 200 m/pixel data (a and b) for the northern half of the scene, north of 20.08°N latitude, and (c and d) for the southern half of the scene. In Figure 13d, "CV" refers to the central valley crater associated with spot "e" in Figure 10a.

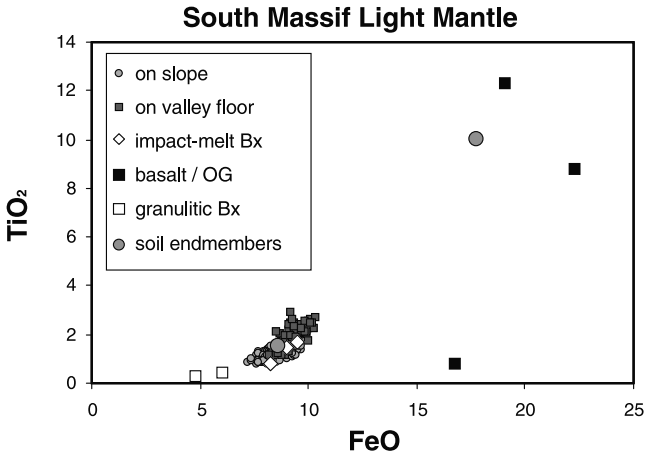

Figure 14. FeO versus TiO_2 (both wt%) derived from topographically corrected data for light mantle at the base of the northern slope of South Massif and extending onto the basaltic plain, compared to the Apollo 17 reference suite (Table 4). As expected from the samples, these materials are strongly dominated by impact-melt breccia of the types sampled at Station 2 (see Figure 10b). Values of FeO and TiO_2 are slightly higher in the light mantle on the valley floor because of some (minor) mixing with basaltic regolith.

impact-melt breccia typical of Apollo 17 samples (Figures 17 and 20b). On lower, southern slopes of South Massif, however, regolith compositions reflect mixing with basaltic materials (Table 5). Whether the basaltic components represent impact ejecta from the surrounding basaltic plains or reflect, at least in part, an older basaltic component is an open question. Evidence of older volcanic plains north of the Sculptured Hills at similar elevations to some of the low-elevation southern slopes of South Massif supports the possibility of an older volcanic component (see below).

[28] North Massif regolith compositions reflect the same feldspathic component as South Massif, but the noritic compositions that presumably signal enrichments of impact-melt deposits differ from those of South Massif (Figure 20). Compositions of one of the noritic "patches" on North Massif (defined by FeO in the 8–11 wt% range) are offset toward higher FeO and lower TiO_2 compared to typical Apollo 17 melt-breccia compositions (Figure 20a). The compositional offset is what would be expected from mixing with a VLT basaltic component. This is an intriguing possibility because of evidence in other areas of the Taurus-Littrow region for VLT basaltic components, such as in the eastern valley (discussed above) and in the Sculptured Hills (see below).

[29] Another key question at the Apollo 17 site relates to the presence or absence of Imbrium ejecta deposits. According to crater ejecta modeling, the Apollo 17 site is close enough to Imbrium that significant ejecta from the Imbrium event ought to be present [*McGetchin et al.*, 1973; *Haskin et al.*, 2000]. The aphanitic impact-melt breccias [*Spudis and Ryder*, 1981] and the incompatible-element-rich (ITE-rich) impact-melt breccias [*Jolliff et al.*, 1996] differ somewhat from the poikilitic breccias and could possibly represent distal Imbrium ejecta components (although the differences are slight compared to differences between the Apollo 17 groups and other Apollo melt-breccia groups [*Jolliff*, 1998]). The Sculptured Hills have a knobby morphology, similar to the Montes Rook Formation of the Orientale basin, which, by analogy, would make them a primary ejecta deposit of the Serenitatis basin (reviewed by *Spudis* [1993]). *Spudis and Ryder* [1981], however, argued on the basis of photogeologic evidence that knobby Sculptured Hills materials overlie the rims of craters such as Le Monnier and Littrow, which are superposed on Serenitatis ring structures, meaning that at least some of these knobby deposits must be younger. *Spudis and Ryder* [1981] suggested that these deposits may be a distal facies of Imbrium ejecta or perhaps a combination of Imbrium and other smaller post-Serenitatis impacts such as Littrow, Vitruvius, and Maraldi. The diversity of impact-melt breccias found at the landing site may be consistent with this idea; that is, the aphanitic and ITE-rich groups may have a non-Serenitatis origin, and Imbrium is likely, especially for the ITE-rich group. On the other hand, a lack of prominent Imbrium-radial lineations in the immediate vicinity (as opposed to Imbrium-grooved terrain north of the site, especially north and east of Crater Littrow), suggests that the Apollo 17 site may lie in a "window" that escaped significant deposition of Imbrium material [see also *Reed and Wolfe*, 1975; *Wilhelms*, 1987, Plate 8]. Even so, *Wilhelms* [1987] allows that the abundance of Imbrium-radial material nearby is consistent with superposition of Imbrium ejecta on the Serenitatis massifs.

[30] The Apollo 17 sample location closest to knobby deposits, station 8, was at the foot of the Sculptured Hills, just across the Wessex Cleft from North Massif (Figure 10). The soil and rock components sampled there are similar to those of Stations 6 and 7, although there appears to be a greater proportion of basaltic debris thrown up from the valley floor [*Korotev and Kremser*, 1992]. There is, however, no assurance that materials sampled at Station 8 or LRV 11 are representative of materials throughout the Sculptured Hills; on the contrary, the Clementine data suggest the possibility of other rock types exposed there, as discussed in section 4.4. Overall, the compositional diversity of the Sculptured Hills material as derived from Clementine data suggests that if it is of Serenitatis origin, it probably repre-

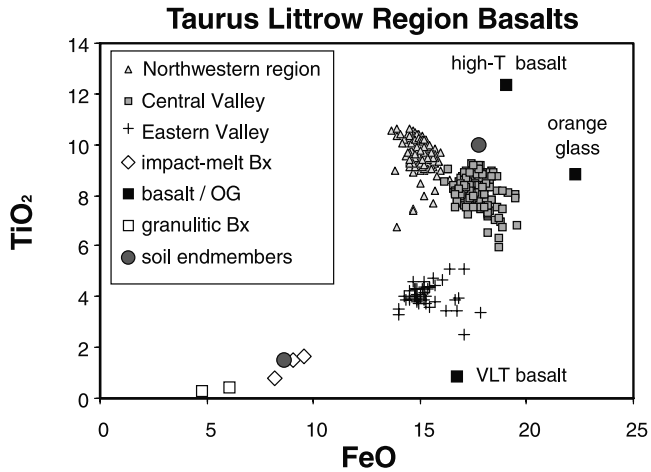

Figure 15. FeO versus TiO_2 (both wt%) for different basaltic areas, central valley, northwestern area, and eastern valley (see also Table 5 and Figure 10).

Table 5. FeO and TiO_2, Corrected for Topography, and Elevations of Selected Areas in the Apollo 17 Region

	Latitude, deg	Longitude, deg	Map Ref.[b]	Number of Pixels	FeO Min	FeO Mean	FeO Max.	FeO St.Dev.	TiO_2 Min.	TiO_2 Mean	TiO_2 Max.	TiO_2 St.Dev.	Elevation,[a] m Min.	Mean	Max.	St.Dev.
Basalt area																
Central Valley	20.116–20.176	30.737–30.843	1	160	16.2	17.6	19.5	0.6	5.9	8.3	9.2	0.6	−6	−2.3	0.5	1.6
Northwest of Family Mountain	20.367–20.453	30.133–30.189	2	126	13.7	15.0	16.3	0.5	6.7	9.6	10.7	0.7	22.8	24.7	25.3	0.5
Eastern Valley	20.017–20.057	31.180–31.215	3	42	14.0	15.3	17.8	0.9	2.5	4.0	5.1	0.5	−27.8	−24.7	−21.7	1.1
South Massif, Light Mantle																
On valley floor	20.123–20.189	30.477–30.540	4	110	8.2	9.3	10.3	0.4	1.2	1.9	2.9	0.4	80	152	198	30
On slope	20.057–20.116	30.449–30.533	5	130	7.2	8.5	9.7	0.6	0.8	1.3	2.0	0.3	122	336	1014	220
South Massif																
Typical noritic	20.031–20.083	30.428–30.540	6	153	7.3	8.5	10.9	0.7	0.7	1.2	2.0	0.3	122	672	1513	355
Typical feldspathic	20.011–20.110	30.273–30.315	7	112	5.6	6.9	9.0	0.6	0.4	0.6	1.0	0.1	703	1501	2291	448
High elevation, Fe-Ti rich	19.925–20.017	30.315–30.393	8	180	6.4	9.9	12.1	1.0	0.6	2.2	3.6	0.6	2032	2263	2376	79
Southern flank, low-elevation	19.747–19.852	30.203–30.315	9	289	10.2	12.0	14.2	0.7	1.8	3.4	5.0	0.7	641	1007	1385	179
North Massif																
Typical noritic	20.334–20.427	30.709–30.828	10	270	7.6	9.7	11.4	0.8	0.3	1.1	2.5	0.8	505	1259	1662	285
Typical feldspathic	20.347–20.420	30.589–30.667	11	144	5.3	7.4	9.4	0.8	0.5	1.0	3.3	0.4	548	1073	1363	195
Sculptured Hills																
Undifferentiated	20.235–20.387	30.927–31.089	12	272	7.7	9.9	13.5	1.0	0.4	1.3	2.5	0.5	909	1103	1252	71
Feldspathic	20.156–20.182	31.046–31.089	13	35	6.2	7.7	9.5	0.8	0.8	1.3	2.1	0.4	368	586	757	97
Mafic anomaly	20.209–20.242	31.075–31.124	14	48	9.7	13.0	16.8	1.8	1.1	1.8	2.5	0.3	649	876	1042	107
High plains unit																
Undifferentiated	20.367–20.446	31.229–31.398	15	325	10.4	11.9	13.5	0.6	1.3	2.9	4.5	0.6	1002	1076	1186	29

[a] Relative to Apollo 17 ALSEP.
[b] Sample areas indicated by numbered boxes in Figure10a.

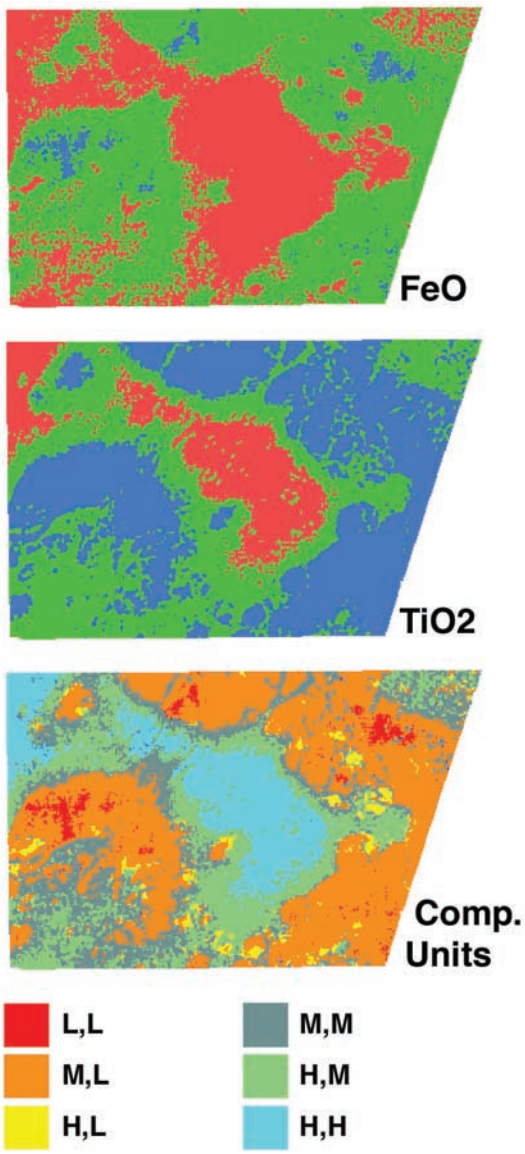

Figure 16. (top) CSR-derived FeO values quantized into three bins (red >12 wt%, green >7 and ≤12 wt%, blue ≤7 wt%), (middle) quantized TiO_2 values (red >6 wt%, green >2 and ≤6 wt%, blue ≤2 wt%), and (bottom) classification map (Compositional Units) derived from the top two panels (data corrected for local topography). The legend applies only to the bottom panel (see Figure 17 for context). Interpretations of units: L,L, feldspathic upper crustal material; M,L, noritic material and impact melt; H,L, FeO-rich, TiO_2-poor rocks (possibly VLT basalt and other material not represented in the Apollo 17 collection); M,M, mixing zone between mare and highlands and in massif deposits of pyroclastic material concentrated in troughs and valleys through downslope movement; H,M, medium TiO_2 basalt (possibly an artifact of mixing of highlands and basalt, especially around the perimeter of Taurus-Littrow Valley); H,H, high-Ti basalt that floods the entire valley. The mixing units (portions of M,M and possibly H,M) may be partially a result of light scattering in the UVVIS instrument, though this issue remains unresolved and controversial [*Robinson et al.*, 1999; *Li et al.*, 1999; *Robinson*, 2001].

sents a different facies or a stage (late) of ejecta compared to the material that makes up the massifs. Having remotely sensed gamma-ray data for Th at sufficiently high resolution, e.g., 1–2 km, might help to resolve this issue; a high Th concentration associated generally with Sculptured Hills terrain, for example, would implicate an Imbrium origin.

4.4. Highlands: Unsampled Rock Types of the Sculptured Hills and High Plains Unit

[31] A region of elevated FeO and TiO_2 occurs in the northeastern corner of the Taurus-Littrow region, centered on 20.41°N latitude and 31.31°E longitude at about 1 km elevation relative to the valley floor (Table 5, Figures 13a, 13b, and 19). This region, which we refer to as a "high plains" unit, was originally mapped as plains material covered in part with a dark mantle; the dark mantle was interpreted as volcanic material, mostly pyroclastic from local vents [*Scott and Carr*, 1972; *Lucchitta*, 1972]. This same unit was later mapped as "plains material" by *Wolfe et al.* [1981], who interpreted it as an early Imbrian polygenetic deposit of mass-wasted debris, crater ejecta, and possibly a volcanic component. The unit was referred to as "smooth highland plains" by *Spudis and Ryder* [1981], who also suggested that it may postdate Sculptured Hills terra. All four previous studies interpret the high plains unit as younger than the Sculptured Hills. A relatively high density of craters suggests to us that it may be older and that Sculptured Hills material may be superposed on this surface. Our compositional analysis confirms the presence of a mafic (presumably volcanic) component in the high plains unit [see also *Jolliff*, 1999]; compositional variation is minimal and too mafic to be any known type of impact melt. Locally, where small craters expose the freshest material, FeO and TiO_2 reach 13.5 and 4.5 wt%, respectively. This formation appears to be regolith developed on an old, elevated basaltic or basalt-rich surface. Because of the relatively uniform composition of the plains unit and because small craters do not exhume material of more feldspathic composition, we rule out a significant volcanic ash (i.e., surficial) component as a cause of the mafic composition. Assuming that the unit is composed of basalt mixed with feldspathic nonmare material, the basalt component would appear to be of intermediate TiO_2 composition (e.g., 4–8 wt% TiO_2 at 20 wt% FeO). Representatives of this material have not been found among the Apollo 17 samples. A relatively high density of craters suggests that the high plains unit represents an old surface, perhaps predating the Serenitatis impact (similar material may fill Littrow crater to the north with deposits resembling Sculptured Hills material superposed on it (see geologic map of *Wolfe et al.* [1981])). The elevation of the plains unit north of the Sculptured Hills is similar to other plains deposits farther north and in Crater Littrow as well as to the plains on the western edge of Palus Somni and in Sinus Amoris to the east and northeast of the Taurus-Littrow region [*NASA*, 1974]. Alternatively, this surface may be an early "scour" facies or thin plains deposit of the Serenitatis basin impact left uncovered by later ejecta deposits, but where the older surface was basaltic. If this were the case, clasts of such basalts might be expected to occur in Apollo 17 breccias. Indeed, basaltic clasts are found in Apollo 17 breccias, but they are rare in the poikilitic impact-melt rocks [*Spudis and Ryder*, 1981].

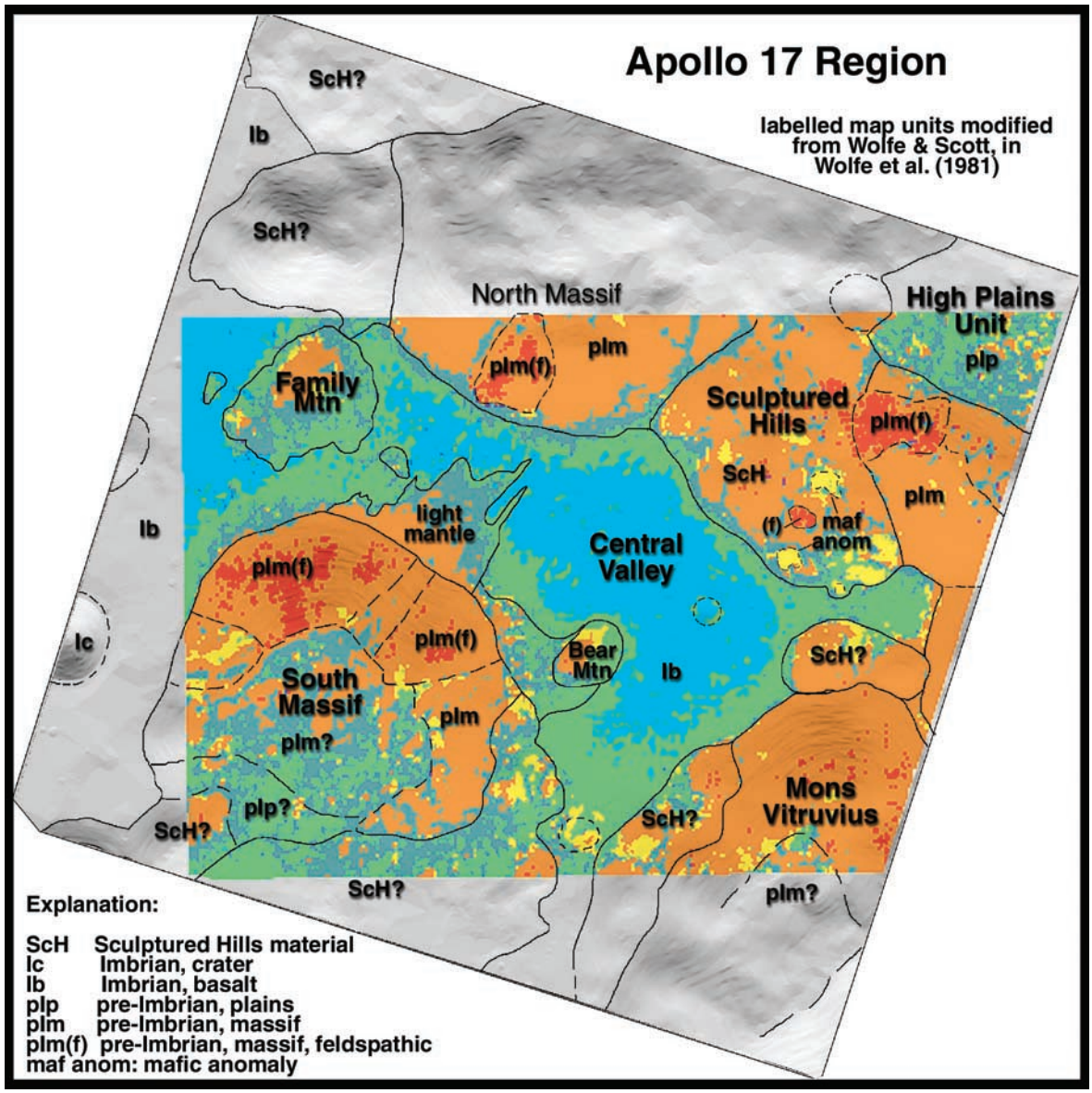

Figure 17. Simplified geologic units map modified from *Wolfe et al.* [1981] with chemical classification map (Figure 16) overlaid.

[32] The southern slope of South Massif has a sculptured texture coupled with elevated FeO and TiO_2, especially in local topographic lows. One possibility is that this surface is enriched in pyroclastic material and that local slopes and mass-wasting processes have produced a focusing effect, concentrating regolith rich in volcanic ash into local troughs. Another possibility is suggested by the observation that compositions are similar to those of the high plains unit. The deposits on the southern part of South Massif, although more variable in composition and topography, occur at about 500–800 m above mare basaltic plains, with elevated FeO and TiO_2, and separated by as much as 5–6 km lateral distance from the nearest mare basalt surfaces. This distance exceeds that of the typical mixing profile at mare-highland boundaries in this region, which, judging from the massif profiles (Figures 17 and 18), is about 1–3 km laterally. We suggest the possibility that these areas of elevated FeO and TiO_2 may be remnants of the older surface that is preserved in the high plains and that massif material is superposed on top of this surface.

[33] The Sculptured Hills remain an enigmatic formation in the Taurus-Littrow region. Although their origin was attributed early on to formation of the Serenitatis basin [*Wolfe et al.*, 1981], or, more precisely, the southern Serenitatis basin [*Reed and Wolfe*, 1975], some workers have suggested on the basis of remotely sensed information that these represent a more variable highlands formation, older than the Serenitatis massifs [e.g., *Weitz et al.*, 1998], As discussed in section 4.3, it has also been suggested that the Sculptured Hills may represent the widespread knobby formation that, from relationships seen along the eastern edge of the Serenitatis basin, can also be argued as younger than the massifs and even in some places directly superposed on massif structures [e.g., *Spudis and Ryder*, 1981; *Spudis*, 1993] as well as on the high plains unit.

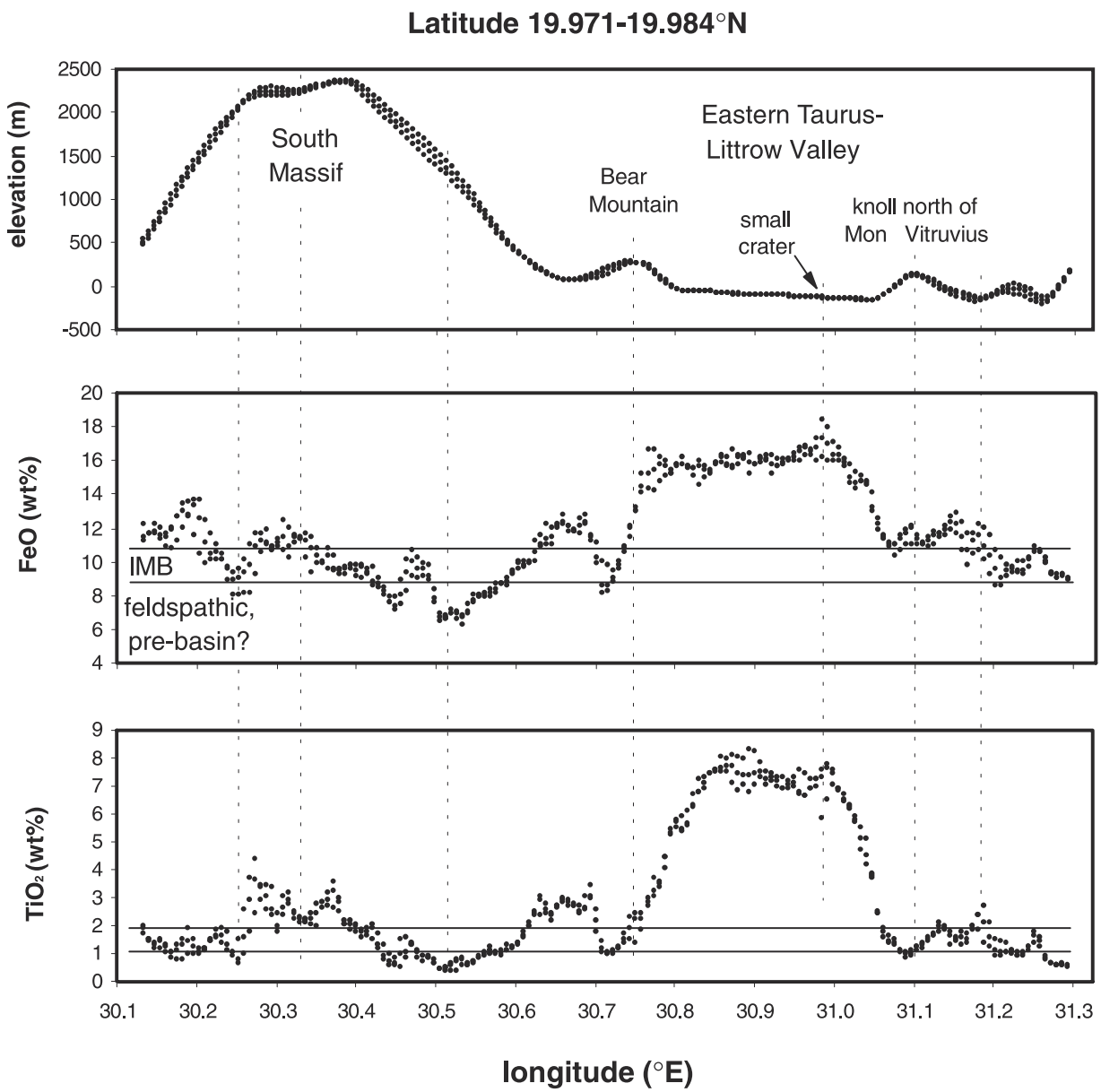

Figure 18. Elevation and compositional profiles along three lines of latitude centered at 19.978°N, extending across South Massif, Bear Mountain, the eastern part of Taurus-Littrow Valley, and to just beyond the northern foot of Mons Vitruvius. Elevation is in meters relative to the Apollo 17 LM. Horizontal lines reflect the approximate compositional range of impact-melt breccia (IMB) (~9–11 wt% FeO, 1–2 wt% TiO_2), with mare basalt dominating regolith at higher concentrations and feldspathic, presumably prebasin materials dominating regolith at lower concentrations. Vertical dashed lines facilitate comparison of compositional "anomalies." Areas near the top of South Massif where TiO_2 concentrations are 3–4% and FeO 11–12% are probably areas where volcanic ash is concentrated. Locally, at both high and intermediate elevations, patches of regolith of FeO and TiO_2 less than that of impact-melt breccia reflect feldspathic material exposed along SW-NE trending features (e.g., at 30.25°E, 30.45°E, and 30.52°E) associated with secondary impacts that also produced the light mantle. That no significant relief corresponds to these compositional variations suggests that they are surficial effects (similar to rays) and not directly related to large-scale massif stratigraphy. Compositional asymmetry about Bear Mountain reflects the effect of mixing of basalt from the east (impacts into the valley floor).

[34] Because of the irregular, knobby structural fabric of the Sculptured Hills, high-resolution topographic corrections are essential to interpretations based on CSR-derived FeO and TiO_2. From the topographically corrected data (see Table 5) it is evident that compositions vary substantially, ranging from feldspathic (e.g., 6% FeO, <1% TiO_2) to significantly mafic (>15% FeO). Compositions like those of noritic impact-melt breccia are common (e.g., 10% FeO, 1.3% TiO_2), suggesting a significant impact-melt component and, like the massifs, an origin as part of a basin-ejecta

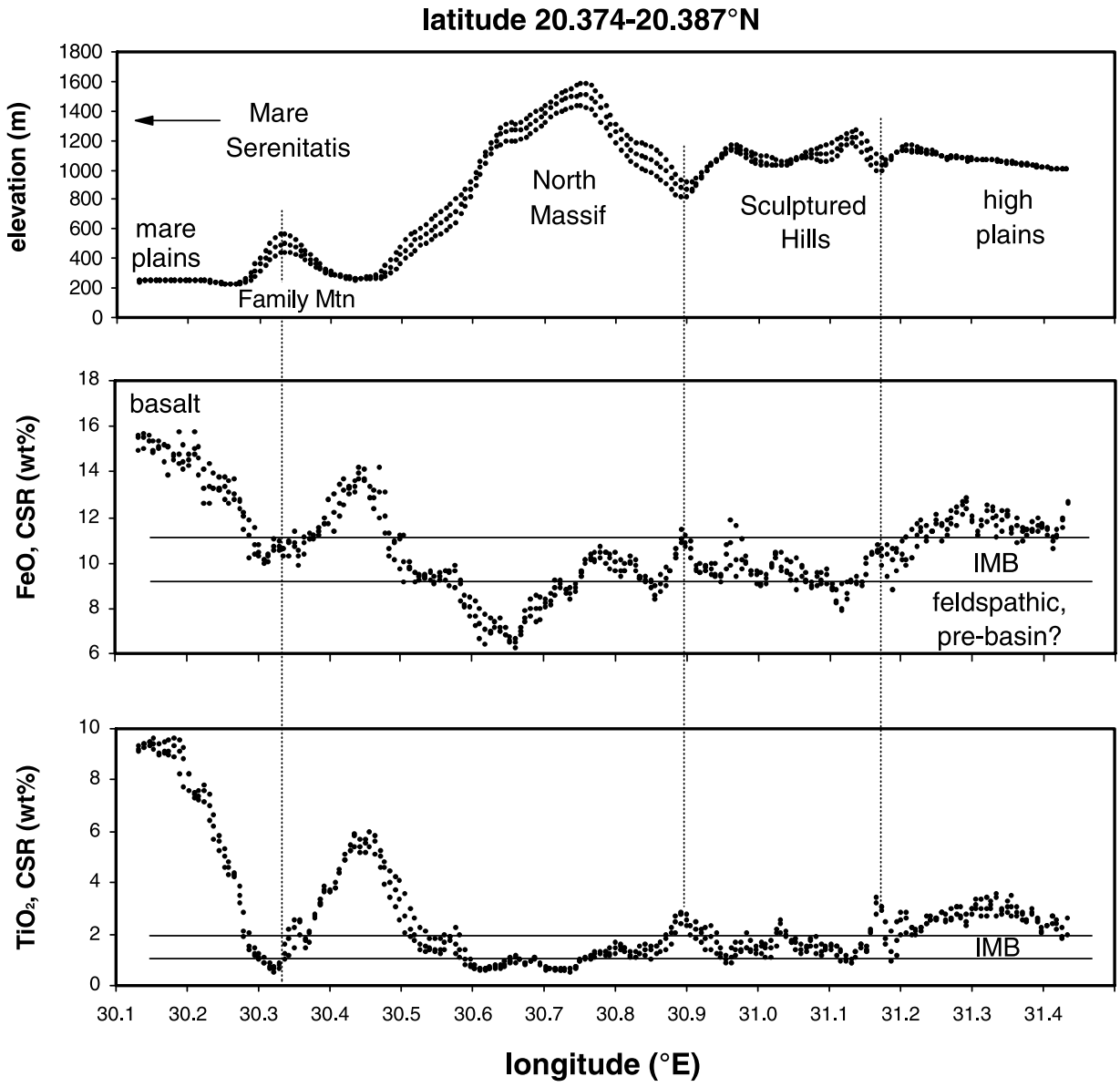

Figure 19. Profile across Family Mountain, North Massif, Sculptured Hills, and high plains unit. Each profile includes three strips of data (100 m resolution) centered on latitude 20.38°N (20.374°, 20.380°, 20.387°). IMB is impact-melt breccia, and bands on FeO and TiO_2 profiles show the typical range of compositions. The range for ''feldspathic, prebasin'' materials lies below the IMB range.

deposit. Small mafic anomalies, however, occur in several locations, most prominently at latitude 20.23°, longitude 31.10° (Figure 10). Here, FeO averages 15 wt% and reaches a maximum of nearly 17 wt%. This particular anomaly occurs on the southeastern slope of a hill at elevation 1735.69 km, about 1100 m above the adjacent valley floor, where the topography precludes contamination from mare basalt of the valley floor. Furthermore, the anomaly is focused and restricted to an area only about 2 km across (Figure 22); thus it seems unlikely to be an ejecta deposit. The ferrous absorption occurs shortward of 1000 nm and appears to be dominated by pyroxene (Table A3). We speculate that this feature may be a small pyroclastic vent or minor effusive flow, and although no cone is apparent, there appear in the Apollo 17 panoramic images (at the limit of resolution) to be small rilles downslope, away from the strongest part of the anomaly. A plot of FeO versus TiO_2 for representative areas within the Sculptured Hills shows soils developed on the mafic anomaly to project directly toward the composition of very low Ti basalt fragments found as small rock fragments in the Apollo 17 soils [see *Jolliff et al.*, 1996]. Confirmation of this feature as volcanic must await future exploration and higher-resolution images.

[35] Another kind of mafic anomaly occurs in the southern part of the Sculptured Hills as fresh bright features exposed on slopes of several small knobs. The most prominent of these occurs as a high-albedo feature in the Apollo pan images as well as in the Clementine 750 nm image and was first identified by *Lucchitta* [1972]. This feature, located at latitude 20.12° and longitude 31.04° (Figures 23 and 24), is small, several hundred meters across, and is situated (crops out?) on the south

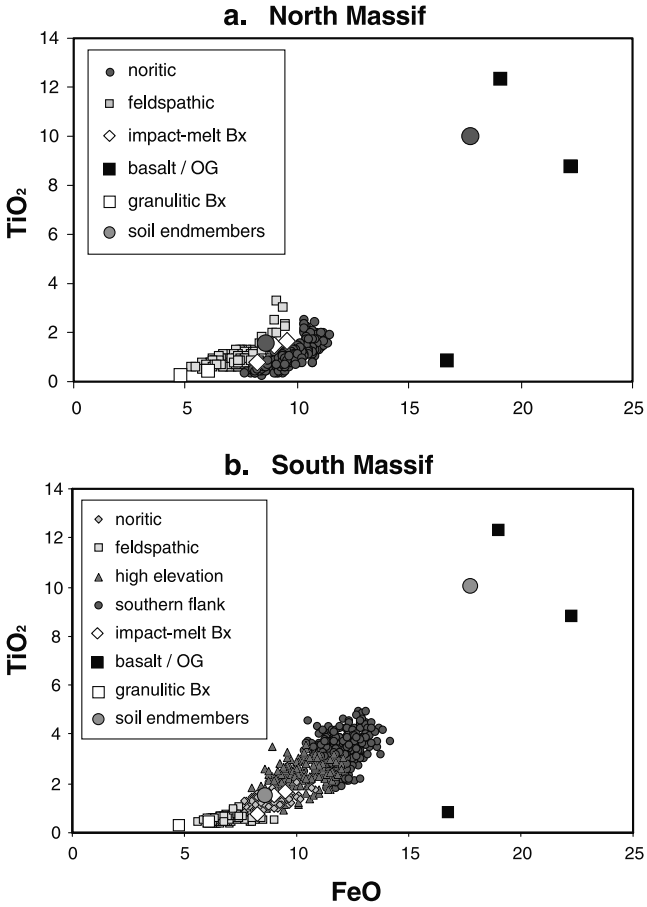

Figure 20. FeO versus TiO_2 (both wt%) for areas on prominent highland massifs. (a) FeO versus TiO_2 for subsampled areas of North Massif that appear to be mainly feldspathic or mainly noritic in composition. A subset of the feldspathic area has several data points with high TiO_2; these may represent a local concentration of volcanic glass. The "noritic" area has slightly higher FeO and lower TiO_2 than expected, perhaps indicating the presence of a VLT basalt component. (b) FeO versus TiO_2 for different regions that represent the compositional diversity on South Massif. None of these areas contains a single lithology; they are soil mixtures. At high elevations, soils are more mafic than the most mafic noritic impact-melt breccias from the landing site, indicating the presence of a basalt component, and relatively high Ti/Fe (spurious) suggests a high-Ti pyroclastic-glass component. This area is near the top of the massif. Mafic compositions on the southern flank may have a different basalt component (see text).

facing slope of a hill and has very sharp contacts with adjacent regolith. The morphology of this relatively high reflectance material includes fingers that extend straight downslope and appear to have formed by mass wasting of a local exposure of rock at the top of the feature. Although the feature has high albedo, it has a moderately strong ferrous absorption, with corresponding FeO concentration of 13.7 wt% and <1 wt% TiO_2, and is dominated by pyroxene (Table A3). Its relatively high albedo and moderately high FeO result from its relative immaturity (Figure 4). Its composition is intermediate between feldspathic highlands material and VLT basalt. The restricted size of the feature and its sharp contacts with surroundings indicate that it is most likely to be the surface expression of a recently exposed FeO rich rock, possibly emplaced as a large block during formation of the Serenitatis basin (or even emplacement of Imbrium ejecta). *Lucchitta* [1972] proposed that the material might be excavated material or local volcanic material.

5. Summary and Conclusions

[36] Steep slopes such as those that characterize the highland massifs and the Sculptured Hills at the Apollo 17 site have a strong effect on compositional information derived from Clementine UVVIS data. Although topography-related effects tend to cancel when the scale of resolution is large compared to the scale of the topography, the effects are significant at high resolution. Derived concentrations of FeO and TiO_2 may be in error by as much as 4–5 wt% (absolute) on slopes facing directly away from or toward the Sun. In photometrically uncorrected data, such variations can lead to erroneous interpretations of rock types and rock-type diversity within highland geologic formations.

[37] In addition to correcting for slope-related errors in compositional derivations, high-resolution digital elevation data are also extremely useful in the interpretation of compositional variations. Correlations between composition and elevation indicate geologic units and stratigraphy. Areas of elevated plains that are compositionally distinctive, such as the "high plains unit," correlate to similar plains materials north of the Taurus-Littrow region but may also correlate to compositionally similar material at similar elevations in the region, but lacking the smooth-plains morphology. In the Apollo 17 region the compositional data suggest that these areas contain an old volcanic component and are not simply smooth plains associated with basin formation and ejecta. At the landing site, however, it appears that this component was not sampled.

[38] Compositional studies of deposits that have significant local relief must be corrected topographically to enable high-resolution definition of regolith and rock units. At the

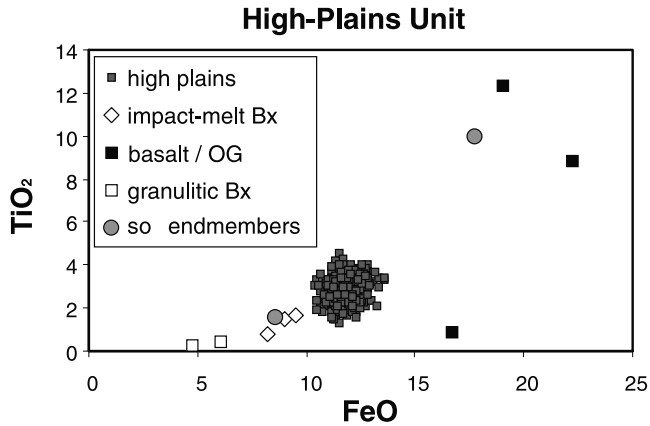

Figure 21. FeO versus TiO_2 (both wt%) of high plains unit (20.41° latitude, 31.31° longitude; see Figure 10, Table A3). The data points form a tight cluster and project to an intermediate TiO_2 concentration basaltic (FeO-rich) component.

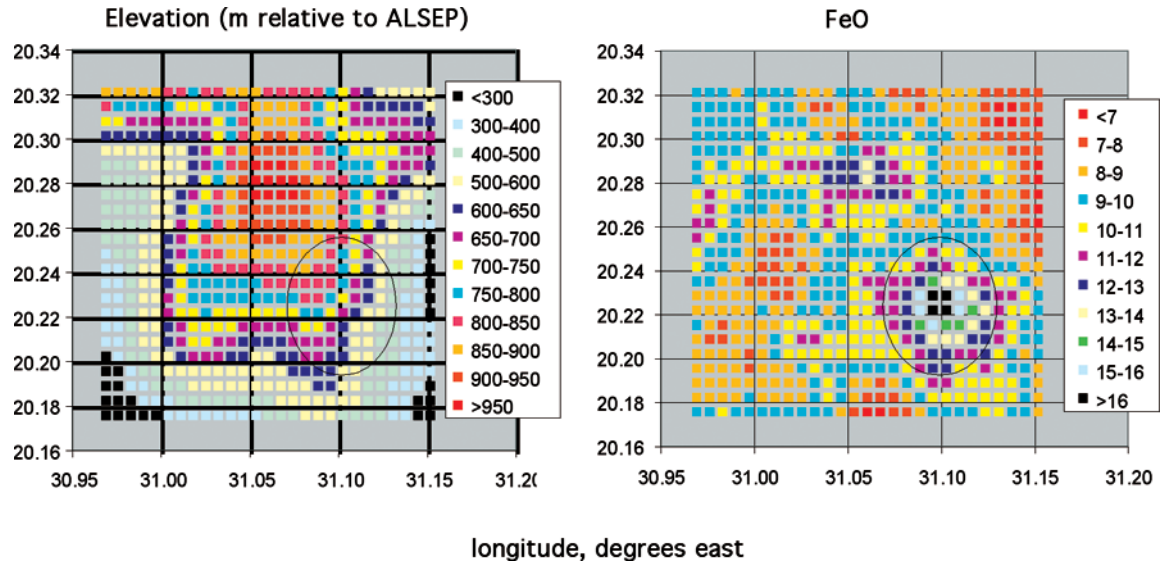

Figure 22. Sculptured Hills mafic anomaly located at 20.22°N latitude, 31.10°E longitude: (a) map view zoom of topography and (b) same field of view for FeO (both wt%) (Figure 10a, box 14, Table 5).

Apollo 17 site, the full range of compositional variability can be determined with the confidence that the feldspathic areas are not simply a result of slope-related brightening and that the more mafic areas are not simply a result of slope-related darkening. Observed variations are consistent with the occurrence of a chaotic mixture of impact melt and more feldspathic material, as indicated by massif materials brought to the edge of the valley floor by downslope mass wasting, and areas of volcanic ash deposits on the tops of the massifs and concentrated in troughs and draws by downslope movement associated with mass wasting [*Lucchitta*, 1972]. The Sculptured Hills have compositions that are similar to areas on the massifs corresponding to noritic impact-melt breccia; however, they lack regolith as feldspathic as some areas of the massifs, and they include several mafic anomalies that may correspond to small, isolated volcanic or exposed hypabyssal features (Figure 24). Alternatively, these observations support the idea that the Sculptured Hills represent a facies of the Imbrium ejecta that was rich in basaltic materials. Further, the age relations between the Sculptured Hills and the high plains unit is not clear; convincing arguments can be made that the Sculptured Hills superpose the high plains unit (see above).

[39] This combined high-resolution composition-topography investigation leads to detailed hypotheses or questions that could be tested or addressed with further exploration, human or robotic, in situ or sample-return, at this or other locations. Learning how and when the high plains unit and Sculptured Hills–like terrain formed would increase our understanding of the stratigraphy and timing of deposits associated with basin impacts and possibly the age and composition of older nonmare volcanic materials. With this study of the Apollo 17 site we have only scratched the surface of what could be done in the investigation of local geologic features and formations combining full-resolution CSR data along with existing high-resolution topography from Apollo data and more recent Earth-based radar observations [*Margot et al.*, 1999, 2000]. Additional topographic data sets for the Moon are available at resolutions below that of the CSR data (~500–1000 m/pixel [*Oberst et al.*, 1996, 1997; *Cook et al.*, 1996, 2000]). We have shown that topographic-photometric corrections maximize the amount of spectral information obtained from orbital color mapping of the Moon. In order to fully exploit derived spectral parameters of lunar soils (or any planet or asteroid), future high-resolution color imaging should be obtained in conjunction with stereo imaging at a resolution comparable to the spectral data (spatial resolution of derived topography is typically 2–10× lower than the resolution of the stereo images from which it is derived). Such an instrument (High Resolution Stereo Camera [*Neukum et al.*, 1996]) is being flown on board Mars Express and should greatly enhance the scientific interpretation of multispectral color imaging that will be obtained simultaneously with the stereo imaging.

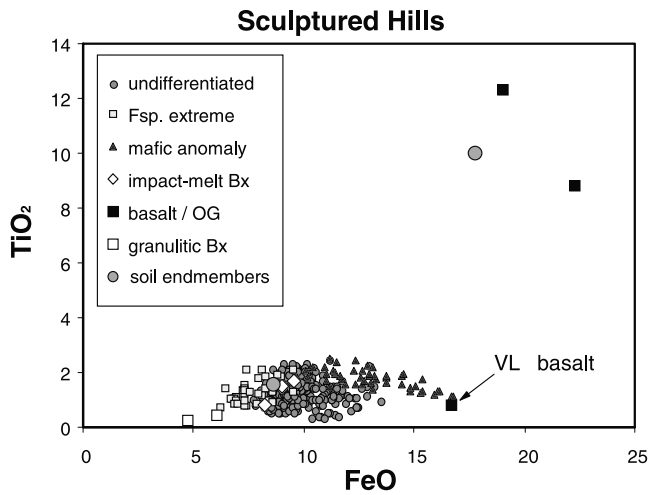

Figure 23. Sculptured Hills FeO versus TiO_2 (both wt%); undifferentiated, feldspathic extreme, mafic anomaly. Data points representing the bright feature discussed in the text are included as "undifferentiated" and occur at 12–13 wt% FeO (Figure 10, Table 5).

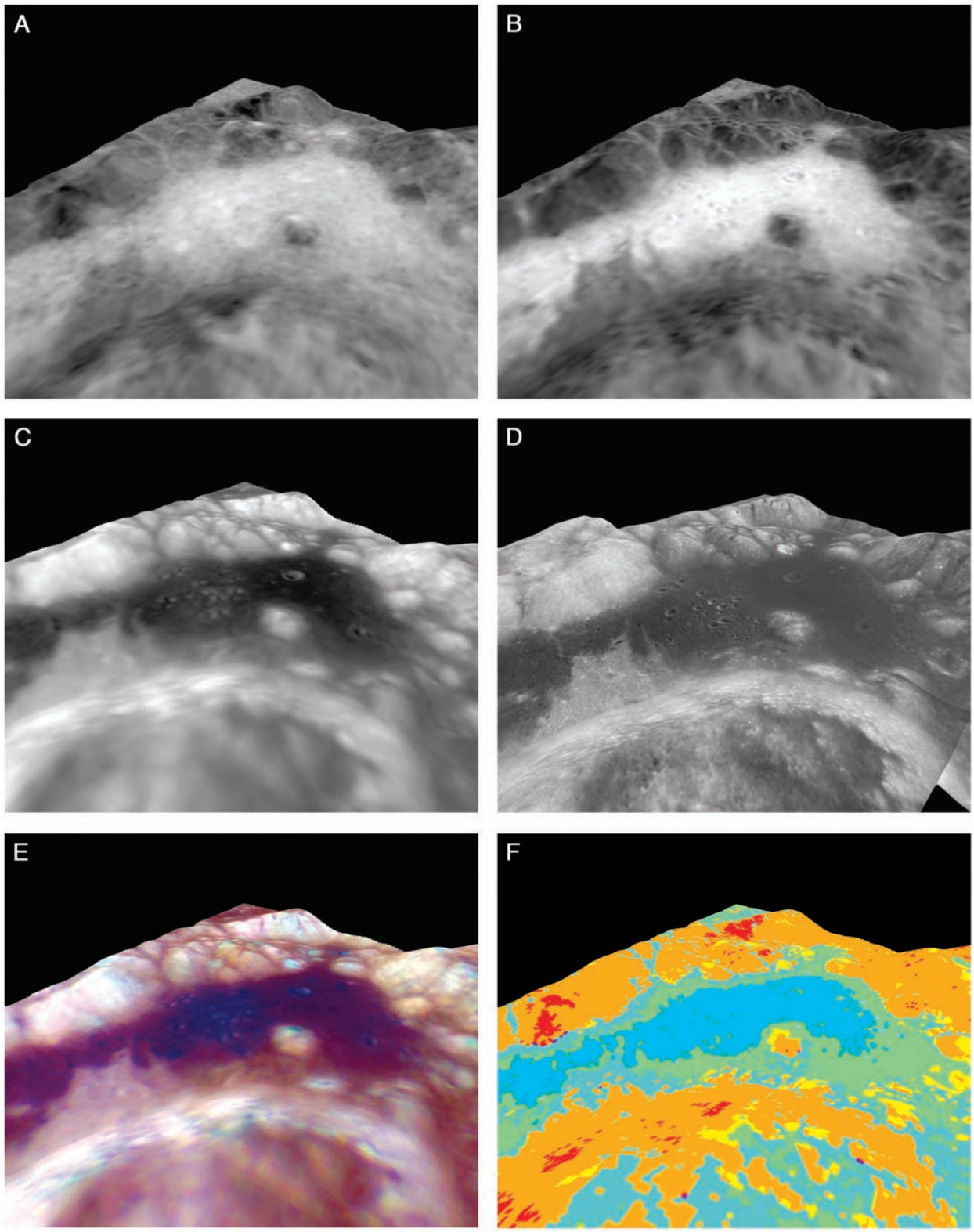

Figure 24. Perspective view of the Taurus-Littrow Valley focusing on sculptured Hills region. (a) FeO, (b) TiO_2, (c) Clementine 750 nm normalized reflectance, (d) Apollo 15 high resolution Pan images (9557–9559), (e) saturation enhanced Clementine three color (950, 750, 415 nm), and (f) chemical classification map (see Figure 16). All images are reprojected to view as seen from position 14 km above lat = 19.75°, lon = 30.2° looking northeast toward lat = 20.29°, lon = 31.84°; see Figure 10 for context.

Appendix A

Table A1. Apollo 17 Sample Station Data, With Photometric Correction for Local Topography

Station	Latitude	Longitude	Sample	Line	Filter	Single Pixel	3 × 3 Avg	3 × 3 St Dev	5 × 5 Avg	5 × 5 St Dev
lm	20.199	30.742	498	246	A	0.0717	0.0718	0.0005	0.0713	0.0008
					B	0.1090	0.1092	0.0011	0.1089	0.0012
					C	0.1149	0.1148	0.0013	0.1143	0.0017
					D	0.1173	0.1163	0.0011	0.1157	0.0013
					E	0.1209	0.1205	0.0008	0.1203	0.0011
S1	20.157	30.754	501	256	A	0.0723	0.0726	0.0015	0.0732	0.0022
					B	0.1073	0.1086	0.0023	0.1101	0.0044
					C	0.1106	0.1119	0.0019	0.1132	0.0031
					D	0.1127	0.1133	0.0019	0.1140	0.0029
					E	0.1155	0.1167	0.0017	0.1177	0.0030
S2	20.099	30.496	428	273	A	0.1168	0.1174	0.0018	0.1177	0.0034
					B	0.1810	0.1813	0.0023	0.1814	0.0052
					C	0.1905	0.1908	0.0030	0.1910	0.0060
					D	0.1950	0.1944	0.0033	0.1944	0.0061
					E	0.2013	0.2015	0.0033	0.2014	0.0067
S3	20.172	30.534	439	251	A	0.1069	0.1057	0.0012	0.1053	0.0019
					B	0.1618	0.1612	0.0043	0.1621	0.0047
					C	0.1716	0.1705	0.0038	0.1712	0.0046
					D	0.1756	0.1744	0.0046	0.1750	0.0056
					E	0.1797	0.1790	0.0046	0.1801	0.0057
S4	20.212	30.598	456	239	A	0.0877	0.0878	0.0023	0.0873	0.0031
					B	0.1367	0.1353	0.0047	0.1346	0.0055
					C	0.1455	0.1445	0.0051	0.1434	0.0061
					D	0.1498	0.1476	0.0049	0.1466	0.0054
					E	0.1546	0.1531	0.0050	0.1519	0.0060
S5	20.183	30.693	484	247	A	0.0684	0.0677	0.0007	0.0677	0.0010
					B	0.1050	0.1044	0.0015	0.1046	0.0022
					C	0.1102	0.1095	0.0013	0.1095	0.0020
					D	0.1125	0.1119	0.0013	0.1116	0.0021
					E	0.1157	0.1155	0.0011	0.1155	0.0021
S6	20.289	30.771	506	216	A	0.0813	0.0820	0.0023	0.0824	0.0035
					B	0.1279	0.1279	0.0034	0.1287	0.0058
					C	0.1356	0.1363	0.0037	0.1371	0.0060
					D	0.1365	0.1387	0.0043	0.1398	0.0066
					E	0.1413	0.1435	0.0038	0.1445	0.0060
S7	20.293	30.785	510	214	A	0.0817	0.0824	0.0032	0.0827	0.0047
					B	0.1289	0.1292	0.0048	0.1299	0.0076
					C	0.1377	0.1380	0.0050	0.1386	0.0080
					D	0.1395	0.1397	0.0050	0.1407	0.0083
					E	0.1451	0.1455	0.0059	0.1460	0.0086
S8	20.278	30.848	528	219	A	0.0797	0.0801	0.0017	0.0806	0.0028
					B	0.1283	0.1289	0.0028	0.1294	0.0042
					C	0.1346	0.1355	0.0025	0.1366	0.0047
					D	0.1385	0.1392	0.0030	0.1398	0.0050
					E	0.1435	0.1444	0.0035	0.1450	0.0055
S9	20.227	30.802	515	234	A	0.0741	0.0742	0.0011	0.0741	0.0020
					B	0.1151	0.1149	0.0032	0.1147	0.0039
					C	0.1205	0.1199	0.0033	0.1198	0.0044
					D	0.1201	0.1209	0.0031	0.1212	0.0044
					E	0.1249	0.1258	0.0036	0.1262	0.0048
LRV1	20.178	30.655	473	249	A	0.0679	0.0679	0.0004	0.0677	0.0004
					B	0.1049	0.1057	0.0007	0.1054	0.0006
					C	0.1116	0.1112	0.0006	0.1111	0.0007
					D	0.1130	0.1129	0.0005	0.1129	0.0004
					E	0.1174	0.1172	0.0006	0.1174	0.0005
LRV2	20.181	30.612	461	248	A	0.0721	0.0719	0.0008	0.0720	0.0010
					B	0.1144	0.1141	0.0018	0.1140	0.0027
					C	0.1225	0.1222	0.0020	0.1220	0.0029
					D	0.1237	0.1233	0.0021	0.1234	0.0028
					E	0.1293	0.1291	0.0018	0.1290	0.0026
LRV3	20.181	30.596	456	248	A	0.0796	0.0796	0.0040	0.0797	0.0063
					B	0.1192	0.1195	0.0054	0.1212	0.0092
					C	0.1277	0.1279	0.0062	0.1294	0.0097
					D	0.1295	0.1297	0.0062	0.1318	0.0104
					E	0.1351	0.1352	0.0062	0.1367	0.0100
LRV4	20.107	30.517	434	270	A	0.1088	0.1089	0.0010	0.1091	0.0013
					B	0.1692	0.1701	0.0020	0.1712	0.0029
					C	0.1807	0.1805	0.0021	0.1810	0.0027
					D	0.1837	0.1840	0.0019	0.1842	0.0025
					E	0.1891	0.1892	0.0022	0.1898	0.0031

Table A1. (continued)

Station	Latitude	Longitude	Sample	Line	Filter	Single Pixel	3 × 3 Avg	3 × 3 St Dev	5 × 5 Avg	5 × 5 St Dev
LRV5	20.184	30.557	445	247	A	0.1043	0.1042	0.0014	0.1037	0.0020
					B	0.1600	0.1601	0.0020	0.1601	0.0025
					C	0.1707	0.1706	0.0017	0.1697	0.0027
					D	0.1735	0.1734	0.0017	0.1725	0.0029
					E	0.1793	0.1793	0.0020	0.1785	0.0030
LRV6	20.194	30.563	447	244	A	0.1026	0.1022	0.0007	0.1020	0.0014
					B	0.1598	0.1584	0.0023	0.1579	0.0027
					C	0.1693	0.1684	0.0024	0.1677	0.0029
					D	0.1717	0.1711	0.0017	0.1705	0.0024
					E	0.1769	0.1766	0.0023	0.1763	0.0028
LRV7	20.213	30.634	467	238	A	0.0705	0.0707	0.0011	0.0711	0.0018
					B	0.1094	0.1102	0.0013	0.1109	0.0021
					C	0.1165	0.1172	0.0016	0.1181	0.0024
					D	0.1186	0.1193	0.0013	0.1206	0.0025
					E	0.1243	0.1246	0.0020	0.1253	0.0029
LRV8	20.203	30.662	475	241	A	0.0674	0.0677	0.0006	0.0680	0.0009
					B	0.1055	0.1060	0.0006	0.1065	0.0020
					C	0.1115	0.1118	0.0007	0.1124	0.0013
					D	0.1134	0.1139	0.0006	0.1143	0.0012
					E	0.1189	0.1193	0.0007	0.1193	0.0011
LRV9	20.233	30.750	500	233	A	0.0690	0.0691	0.0002	0.0693	0.0003
					B	0.1082	0.1086	0.0006	0.1088	0.0010
					C	0.1148	0.1152	0.0004	0.1153	0.0008
					D	0.1163	0.1169	0.0012	0.1172	0.0016
					E	0.1214	0.1215	0.0010	0.1216	0.0014
LRV10	20.283	30.753	501	217	A	0.0881	0.0874	0.0020	0.0867	0.0034
					B	0.1402	0.1372	0.0047	0.1359	0.0060
					C	0.1480	0.1461	0.0041	0.1443	0.0070
					D	0.1525	0.1500	0.0044	0.1480	0.0071
					E	0.1561	0.1542	0.0041	0.1525	0.0067
LRV11	20.276	30.841	526	220	A	0.0767	0.0767	0.0011	0.0775	0.0019
					B	0.1231	0.1232	0.0021	0.1245	0.0035
					C	0.1305	0.1306	0.0021	0.1319	0.0033
					D	0.1326	0.1327	0.0023	0.1343	0.0036
					E	0.1369	0.1370	0.0027	0.1388	0.0041
LRV12	20.197	30.781	509	244	A	0.0735	0.0734	0.0008	0.0731	0.0012
					B	0.1102	0.1105	0.0019	0.1109	0.0026
					C	0.1145	0.1144	0.0013	0.1143	0.0014
					D	0.1128	0.1140	0.0015	0.1147	0.0019
					E	0.1190	0.1192	0.0011	0.1194	0.0013

Table A2. Apollo 17 Sample Station Data, Without Photometric Correction for Local Topography

Station	Latitude	Longitude	Sample	Line	Filter	Single Pixel	3 × 3 Avg	3 × 3 St Dev	5 × 5 Avg	5 × 5 St Dev
lm	20.199	30.742	498	246	A	0.0724	0.0724	0.0006	0.0719	0.0009
					B	0.1101	0.1103	0.0013	0.1098	0.0013
					C	0.1161	0.1159	0.0015	0.1152	0.0018
					D	0.1185	0.1174	0.0012	0.1167	0.0015
					E	0.1222	0.1217	0.0009	0.1213	0.0011
S1	20.157	30.754	501	256	A	0.0727	0.0730	0.0016	0.0735	0.0025
					B	0.1079	0.1091	0.0025	0.1105	0.0049
					C	0.1113	0.1125	0.0021	0.1136	0.0035
					D	0.1134	0.1139	0.0021	0.1144	0.0034
					E	0.1161	0.1173	0.0020	0.1181	0.0035
S2	20.099	30.496	428	273	A	0.1157	0.1162	0.0016	0.1165	0.0025
					B	0.1794	0.1795	0.0018	0.1796	0.0036
					C	0.1888	0.1889	0.0023	0.1891	0.0041
					D	0.1933	0.1924	0.0027	0.1924	0.0042
					E	0.1995	0.1995	0.0025	0.1993	0.0046
S3	20.172	30.534	439	251	A	0.1078	0.1078	0.0009	0.1081	0.0012
					B	0.1632	0.1644	0.0046	0.1663	0.0043
					C	0.1730	0.1740	0.0041	0.1756	0.0042
					D	0.1770	0.1779	0.0049	0.1796	0.0049
					E	0.1812	0.1826	0.0051	0.1847	0.0052
S4	20.212	30.598	456	239	A	0.0879	0.0881	0.0019	0.0877	0.0029
					B	0.1370	0.1358	0.0041	0.1353	0.0052
					C	0.1457	0.1450	0.0044	0.1442	0.0057
					D	0.1501	0.1482	0.0042	0.1474	0.0049
					E	0.1549	0.1536	0.0042	0.1527	0.0056
S5	20.183	30.693	484	247	A	0.0694	0.0692	0.0008	0.0693	0.0010
					B	0.1066	0.1066	0.0018	0.1071	0.0021

Table A2. (continued)

Station	Latitude	Longitude	Sample	Line	Filter	Single Pixel	3 × 3 Avg	3 × 3 St Dev	5 × 5 Avg	5 × 5 St Dev
					C	0.1118	0.1119	0.0011	0.1121	0.0012
					D	0.1141	0.1143	0.0012	0.1142	0.0014
					E	0.1174	0.1180	0.0012	0.1182	0.0015
S6	20.289	30.771	506	216	A	0.0885	0.0891	0.0026	0.0893	0.0040
					B	0.1392	0.1389	0.0039	0.1395	0.0066
					C	0.1475	0.1480	0.0043	0.1485	0.0068
					D	0.1485	0.1506	0.0048	0.1515	0.0074
					E	0.1537	0.1559	0.0043	0.1566	0.0068
S7	20.293	30.785	510	214	A	0.0897	0.0904	0.0034	0.0905	0.0051
					B	0.1415	0.1417	0.0050	0.1421	0.0082
					C	0.1511	0.1513	0.0053	0.1516	0.0086
					D	0.1531	0.1532	0.0053	0.1539	0.0090
					E	0.1593	0.1595	0.0063	0.1597	0.0092
S8	20.278	30.848	528	219	A	0.0787	0.0789	0.0012	0.0793	0.0021
					B	0.1268	0.1270	0.0021	0.1274	0.0031
					C	0.1329	0.1335	0.0017	0.1344	0.0034
					D	0.1368	0.1372	0.0023	0.1376	0.0037
					E	0.1418	0.1423	0.0027	0.1427	0.0042
S9	20.227	30.802	515	234	A	0.0742	0.0741	0.0004	0.0737	0.0006
					B	0.1152	0.1146	0.0021	0.1140	0.0021
					C	0.1206	0.1196	0.0020	0.1191	0.0023
					D	0.1202	0.1206	0.0017	0.1205	0.0023
					E	0.1250	0.1255	0.0021	0.1254	0.0027
LRV1	20.178	30.655	473	249	A	0.0683	0.0682	0.0004	0.0680	0.0004
					B	0.1054	0.1062	0.0007	0.1059	0.0006
					C	0.1121	0.1117	0.0006	0.1116	0.0007
					D	0.1135	0.1134	0.0005	0.1135	0.0005
					E	0.1180	0.1177	0.0006	0.1179	0.0005
LRV2	20.181	30.612	461	248	A	0.0725	0.0723	0.0008	0.0724	0.0010
					B	0.1151	0.1147	0.0018	0.1146	0.0027
					C	0.1233	0.1228	0.0020	0.1226	0.0029
					D	0.1244	0.1240	0.0021	0.1241	0.0028
					E	0.1300	0.1298	0.0018	0.1296	0.0026
LRV3	20.181	30.596	456	248	A	0.0801	0.0801	0.0041	0.0802	0.0064
					B	0.1200	0.1202	0.0056	0.1220	0.0094
					C	0.1285	0.1287	0.0064	0.1303	0.0099
					D	0.1303	0.1305	0.0064	0.1326	0.0106
					E	0.1359	0.1361	0.0064	0.1376	0.0102
LRV4	20.107	30.517	434	270	A	0.1104	0.1106	0.0008	0.1106	0.0010
					B	0.1717	0.1726	0.0017	0.1736	0.0025
					C	0.1833	0.1832	0.0017	0.1835	0.0022
					D	0.1863	0.1868	0.0015	0.1868	0.0021
					E	0.1918	0.1920	0.0019	0.1924	0.0027
LRV5	20.184	30.557	445	247	A	0.1042	0.1042	0.0010	0.1042	0.0017
					B	0.1600	0.1601	0.0012	0.1609	0.0019
					C	0.1706	0.1706	0.0007	0.1705	0.0019
					D	0.1734	0.1734	0.0009	0.1733	0.0022
					E	0.1792	0.1792	0.0010	0.1793	0.0022
LRV6	20.194	30.563	447	244	A	0.1032	0.1028	0.0004	0.1024	0.0010
					B	0.1607	0.1592	0.0018	0.1585	0.0022
					C	0.1702	0.1693	0.0019	0.1683	0.0023
					D	0.1726	0.1720	0.0012	0.1711	0.0019
					E	0.1778	0.1776	0.0017	0.1769	0.0022
LRV7	20.213	30.634	467	238	A	0.0705	0.0706	0.0011	0.0711	0.0018
					B	0.1094	0.1102	0.0013	0.1110	0.0021
					C	0.1164	0.1171	0.0016	0.1181	0.0024
					D	0.1185	0.1193	0.0013	0.1206	0.0025
					E	0.1242	0.1246	0.0019	0.1254	0.0029
LRV8	20.203	30.662	475	241	A	0.0678	0.0681	0.0006	0.0683	0.0007
					B	0.1062	0.1065	0.0005	0.1069	0.0016
					C	0.1121	0.1124	0.0006	0.1129	0.0009
					D	0.1141	0.1145	0.0005	0.1147	0.0008
					E	0.1196	0.1199	0.0006	0.1198	0.0008
LRV9	20.233	30.750	500	233	A	0.0693	0.0695	0.0002	0.0697	0.0003
					B	0.1088	0.1091	0.0005	0.1093	0.0009
					C	0.1155	0.1157	0.0003	0.1158	0.0007
					D	0.1169	0.1175	0.0010	0.1178	0.0015
					E	0.1220	0.1221	0.0008	0.1222	0.0012
LRV10	20.283	30.753	501	217	A	0.0944	0.0935	0.0022	0.0926	0.0039
					B	0.1502	0.1468	0.0052	0.1452	0.0068
					C	0.1585	0.1563	0.0045	0.1542	0.0078
					D	0.1633	0.1605	0.0048	0.1582	0.0079
					E	0.1672	0.1650	0.0045	0.1630	0.0075

Table A2. (continued)

Station	Latitude	Longitude	Sample	Line	Filter	Single Pixel	3 × 3 Avg	3 × 3 St Dev	5 × 5 Avg	5 × 5 St Dev
LRV11	20.276	30.841	526	220	A	0.0768	0.0769	0.0005	0.0773	0.0011
					B	0.1234	0.1235	0.0009	0.1242	0.0020
					C	0.1308	0.1309	0.0006	0.1315	0.0015
					D	0.1329	0.1330	0.0010	0.1339	0.0019
					E	0.1372	0.1373	0.0012	0.1384	0.0023
LRV12	20.197	30.781	509	244	A	0.0740	0.0739	0.0009	0.0737	0.0013
					B	0.1109	0.1112	0.0020	0.1117	0.0029
					C	0.1153	0.1152	0.0014	0.1151	0.0016
					D	0.1136	0.1147	0.0016	0.1156	0.0021
					E	0.1198	0.1201	0.0012	0.1202	0.0015

Table A3. Spectral Reflectance Data for Selected Locations Before and After Photometric Correction for Topography[a]

					Uncorrected		Corrected	
Location	Map	Lat	Lon	Value	3 × 3 Avg	5 × 5 Avg	3 × 3 Avg	5 × 5 Avg
N. Massif, SE slope	a	20.374	30.786	415 nm	0.1378	0.1377	0.1225	0.1221
				750 nm	0.2107	0.2111	0.1873	0.1873
				900 nm	0.2172	0.2171	0.1931	0.1925
				950 nm	0.2203	0.2197	0.1958	0.1948
				1000 nm	0.2288	0.2285	0.2034	0.2026
				FeO	9.0	9.3	10.4	10.7
				TiO,	0.9	0.9	1.4	1.4
S. Massif, W slope	b	19.971	30.161	415 nm	0.0805	0.0801	0.1159	0.1147
				750 nm	0.1281	0.1272	0.1844	0.1821
				900 nm	0.1319	0.1312	0.1899	0.1879
				950 nm	0.1329	0.1321	0.1914	0.1892
				1000 nm	0.1395	0.1385	0.2009	0.1983
				FeO	15.7	15.8	11.1	11.2
				TiO_2	3.6	3.8	1.0	1.0
S. Massif, SE slope	c	19.761	30.561	415 nm	0.1194	0.1192	0.1052	0.1052
				750 nm	0.1862	0.1861	0.1640	0.1641
				900 nm	0.1962	0.1957	0.1728	0.1727
				950 nm	0.1996	0.1992	0.1758	0.1757
				1000 nm	0.2057	0.2052	0.1812	0.1810
				FeO	8.6	8.7	10.1	10.2
				TiO_2	1.2	1.2	1.9	1.9
S. Massif, S. flank	d	19.714	30.175	415 nm	0.0875	0.0880	0.0789	0.0793
				750 nm	0.1382	0.1388	0.1247	0.1252
				900 nm	0.1477	0.1484	0.1333	0.1339
				950 nm	0.1509	0.1518	0.1361	0.1369
				1000 nm	0.1557	0.1567	0.1405	0.1414
				FeO	10.6	10.3	12.0	11.8
				TiO_2	3.0	3.0	4.2	4.2
C.V. Crater, NW rim	e	20.050	30.913	415 nm	0.0761	0.0753	0.0679	0.0688
				750 nm	0.1144	0.1146	0.1020	0.1048
				900 nm	0.1191	0.1187	0.1062	0.1085
				950 nm	0.1195	0.1190	0.1065	0.1088
				1000 nm	0.1230	0.1226	0.1097	0.1121
				FeO	16.8	17.1	18.2	18.2
				TiO_2	7.6	7.0	9.9	8.7
Sc. Hills, slope	f	20.281	31.025	415 nm	0.0984	0.0985	0.1230	0.1213
				750 nm	0.1612	0.1618	0.2015	0.1993
				900 nm	0.1663	0.1658	0.2078	0.2042
				950 nm	0.1672	0.1671	0.2090	0.2058
				1000 nm	0.1723	0.1726	0.2154	0.2125
				FeO	12.8	13.0	10.0	10.4
				TiO_2	1.1	1.0	0.4	0.4
Sc. Hills, feldspathic	g	20.253	31.007	415 nm	0.0936	0.0942	0.1099	0.1104
				750 nm	0.1544	0.1552	0.1811	0.1821
				900 nm	0.1636	0.1644	0.1919	0.1928
				950 nm	0.1673	0.1683	0.1963	0.1974
				1000 nm	0.1727	0.1734	0.2027	0.2034
				FeO	9.9	9.8	7.9	7.9
				TiO_2	1.2	1.2	0.6	0.6
Sc. Hills, mafic	h	20.215	31.096	415 nm	0.1089	0.1080	0.0998	0.0993
				750 nm	0.1761	0.1732	0.1613	0.1592
				900 nm	0.1752	0.1733	0.1606	0.1593
				950 nm	0.1766	0.1746	0.1618	0.1605
				1000 nm	0.1815	0.1796	0.1663	0.1651
				FeO	13.7	13.6	14.7	14.6
				TiO_2	0.9	1.1	1.3	1.5

Table A3. Spectral Reflectance Data for Selected Locations Before and After Photometric Correction for Topography[a]

Location	Map	Lat	Lon	Value	Uncorrected		Corrected	
					3 × 3 Avg	5 × 5 Avg	3 × 3 Avg	5 × 5 Avg
Sc. Hills SW, light halo	i	20.115	31.044	415 nm	0.1554	0.1476	0.1606	0.1515
				750 nm	0.2352	0.2251	0.2432	0.2312
				900 nm	0.2151	0.2098	0.2223	0.2154
				950 nm	0.2138	0.2096	0.2209	0.2151
				1000 nm	0.2209	0.2166	0.2282	0.2223
				FeO	14.1	13.7	13.7	13.4
				TiO_2	0.7	0.7	0.6	0.7

[a] Sc., sculptured; S., south; W, west; NW, northwest; SE, southeast; C.V., Central Valley; $n \times n$ Avg, size of pixel box averaged to determine value; Map, location shown of Figure 10a.

[40] The magnitude of the topographic correction on the derived compositional parameters (FeO and TiO_2), summarized in Figure 5, is asymmetrically disposed relative to incidence angle and emission angles. Figure A1 shows that the topographic correction of normalized I/F (30° incidence, 0° emission) is similar in shape for all three wavelengths studied here but exhibits a smaller percentage change on the 415 nm bandpass. In all four panels of Figure A1 the axes represent residuals from the topographically corrected parameter minus the same parameter derived assuming a spherical Moon at a particular wavelength (Topo-NoTopo). These same data are shown in image form in Figures 2 and 3. To allow inspection of the relative significance of the topographically induced changes in both incidence and emission angles, we made two extra versions of the 750 nm frame, holding incidence angle constant in one and emission angle constant in the other. The ratio of the fully topographically corrected 750 nm frame to the partially corrected frames (the *x* axis is incidence angle, and the *y* axis is emission angle) is shown in Figure A2.

[41] Detailed data values for DEM topographically-photometrically normalized I/F and conventionally photometrically normalized I/F for the Apollo 17 sample stations are presented in Tables A1 and A2, respectively. The data are listed as single-pixel, three-pixel, and five-pixel box averages to show the relatively small pixel-to-pixel variation at each station. Similar data for scientifically significant regions away from the Apollo stations are listed in Table A3.

[42] **Acknowledgments.** We thank J. Gillis (Washington University) for discussion and for assistance with manipulation of Clementine data and K. Edwards (Q&D Programming) for programming assistance. T. Hare

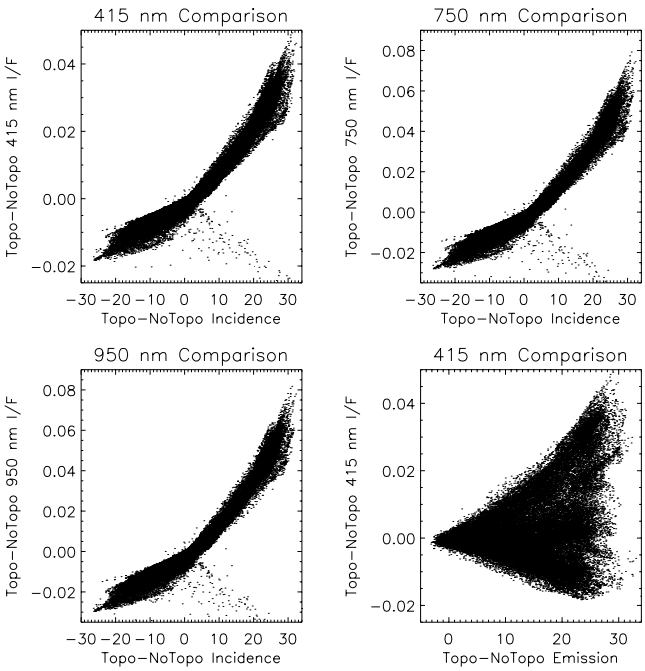

Figure A1. (top left) The *x* axis represents change in incidence angle after applying DEM topographic correction in the photometric normalization; the *y* axis represents 415 nm I/F residual. (top right) Same plot shown at top left with *y* axis showing 750 nm I/F residual. (bottom left) Same as first two plots but with 950 nm I/F residual. (bottom right) Assuming a spherical Moon, the emission angle is close to zero for the entire image; thus residual emission angle is always positive. Data plotted for the 415 nm bandpass.

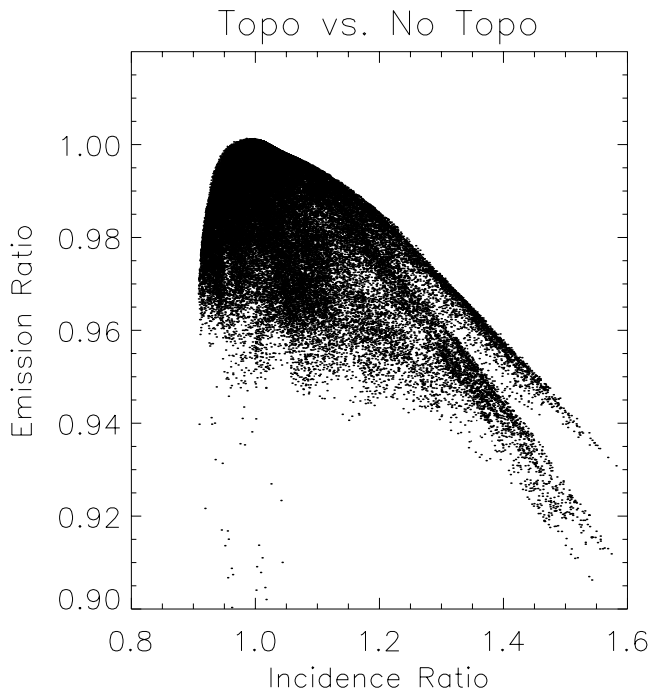

Figure A2. The *x* axis represents the ratio of fully topographically corrected 750 nm image over the same image with the incidence angle not topographically corrected (emission angle is corrected for topography). The *y* axis represents the ratio of fully topographically corrected 750 nm image over the same image with the emission angle not topographically corrected (incidence angle is corrected for topography).

(USGS, Flagstaff) digitized the Apollo 17 contour map. P. Spudis (Lunar and Planetary Institute) and J. Oberst (DLR) provided valuable and insightful reviews to this work. We thank the LPI Regional Planetary Image Facility for providing digital scans of Apollo era photography. Much of the processing of the Clementine data was done using ISIS provided by the U.S. Geological Survey, Flagstaff. This work was supported in part by NASA Planetary Geology and Geophysics grants NAG5-10847 (M.R.) and NAG5-8905 (B.J.).

References

Blewett, D. T., P. G. Lucey, B. R. Hawke, and B. L. Jolliff, Clementine images of the lunar sample-return stations: Refinement of FeO and TiO_2 mapping techniques, *J. Geophys. Res.*, *102*, 16,319–16,325, 1997.

Cook, A. C., J. Oberst, T. Roatsch, R. Jaumann, and C. Acton, Clementine imagery: Selenographic coverage for cartographic and scientific use, *Planet. Space Sci.*, *44*, 1135–1148, 1996.

Cook, A. C., T. R. Watters, M. S. Robinson, P. D. Spudis, and D. B. J. Bussey, Lunar polar topography derived from Clementine stereo images, *J. Geophys. Res.*, *105*, 12,023–12,033, 2000.

Elphic, R. C., S. Maurice, D. J. Lawrence, W. C. Feldman, B. L. Barraclough, A. B. Binder, and P. G. Lucey, Lunar Fe and Ti abundances: Comparison of Lunar Prospector and Clementine data, *Science*, *281*, 1493–1496, 1998a.

Elphic, R. C., S. Maurice, D. J. Lawrence, W. C. Feldman, B. L. Barraclough, A. B. Binder, and P. G. Lucey, Lunar Prospector neutron measurements compared to Clementine iron and titanium abundances, in *Workshop on New Views of the Moon: Integrated Remotely Sensed, Geophysical, and Sample Datasets*, edited by B. Jolliff and G. Ryder, pp. 27–29, Lunar and Planet. Inst., Houston, Tex., 1998b.

Elphic, R. C., D. J. Lawrence, W. C. Feldman, B. L. Barraclough, S. Maurice, A. B. Binder, and P. G. Lucey, Lunar rare earth element distribution and ramifications for FeO and TiO_2: Lunar Prospector neutron spectrometer observations, *J. Geophys. Res.*, *105*, 20,333–20,345, 2000.

Feldman, W. C., D. J. Lawrence, R. C. Elphic, D. T. Vaniman, D. R. Thomsen, and B. L. Barraclough, The chemical information content of lunar thermal and epithermal neutrons, *J. Geophys. Res.*, *105*, 20,347–20,363, 2000.

Gaddis, L. R., C. M. Pieters, and B. R. Hawke, Remote sensing of lunar pyroclastic mantling deposits, *Icarus*, *61*, 469–489, 1985.

Gillis, J. J., B. L. Jolliff, and R. E. Elphic, Integrating rock, soil, and remotely sensed TiO_2 concentrations yields a modified algorithm for calculating TiO_2 from Clementine UVVIS data and an improved global assessment of mare basalt TiO_2 distribution, *J. Geophys. Res.*, *107*, doi:10.1029/2001JE001515, in press, 2002.

Haskin, L. A., J. J. Gillis, R. L. Korotev, and B. L. Jolliff, The materials of the lunar Procellarum KREEP Terrane: A synthesis of data from geomorphological mapping, remote sensing, and sample analysis, *J. Geophys. Res.*, *105*, 20,403–20,415, 2000.

Hawke, B. R., C. R. Coombs, L. R. Gaddis, P. G. Lucey, and P. D. Owensby, Spectral reflectance studies of localized dark mantle deposits on the Moon, in *Proceedings of the 19th Lunar and Planetary Science Conference*, pp. 225–268, Cambridge Univ. Press, New York, 1989.

Hawke, B. R., C. R. Coombs, B. A. Campbell, P. G. Lucey, C. A. Peterson, and S. H. Zisk, Remote sensing of regional pyroclastic deposits on the north central portion of the lunar nearside, *Proc. Lunar Planet. Sci. Conf.*, *21st*, 377–389, 1991.

Head, J. W., III, and L. Wilson, Lunar mare volcanism: Stratigraphy, eruption conditions, and the evolution of secondary crusts, *Geochim. Cosmochim. Acta*, *56*, 2155–2175, 1992.

Heiken, D., and D. S. McKay, Petrography of Apollo 17 soils, *Proc. Lunar Sci. Conf.*, *5th*, 843–860, 1974.

Jolliff, B. L., Large-scale separation of K-frac and REEP-frac in the source regions of Apollo impact-melt breccias and a revised estimate of the KREEP composition, *Int. Geol. Rev.*, *10*, 916–935, 1998.

Jolliff, B. L., Clementine UVVIS multispectral data and the Apollo 17 landing site: What can we tell and how well?, *J. Geophys. Res.*, *104*, 14,123–14,148, 1999.

Jolliff, B. L., K. M. Rockow, R. L. Korotev, and L. A. Haskin, Lithologic distribution and geologic history of the Apollo 17 site: The record in soils and small rock particles from the highland massifs, *Meteorit. Planet. Sci.*, *31*, 116–145, 1996.

Korotev, R. L., Concentrations of radioactive elements in lunar materials, *J. Geophys. Res.*, *103*, 1691–1701, 1998.

Korotev, R. L., and D. T. Kremser, Compositional variations in Apollo 17 soils and their relationships to the geology of the Taurus-Littrow site, *Proc. Lunar Planet. Sci. Conf.*, *22nd*, 275–301, 1992.

Lawrence, D. J., W. C. Feldman, B. L. Barraclough, A. B. Binder, R. C Elphic, S. Maurice, and D. R. Thomson, Global elemental maps of the Moon: The Lunar Prospector gamma-ray spectrometer, *Science*, *281*, 1484–1489, 1998.

Lawrence, D. J., W. C. Feldman, B. L. Barraclough, A. B. Binder, R. C. Elphic, S. Maurice, M. C. Miller, and T. H. Prettyman, Thorium abundances on the lunar surface, *J. Geophys. Res.*, *105*, 20,307–20,331, 2000.

Lee, E. M., et al., Clementine UVVIS multispectral processing (abstract), *Lunar Planet. Sci.*, *XXVIII*, 797–798, 1997.

Li, L., J. F. Mustard, and C. M. Pieters, The effects of scattered light in the Clementine UV-VIS camera on mixture analysis, *Lunar Planet. Sci.*, *XXX*, abstract 1866, 1999.

Lucchitta, B. K., Geologic map of part of the Taurus-Littrow region of the Moon Apollo 17 pre-mission map, *U.S. Geol. Surv. Map I-800*, scale 1:50,000, 1972.

Lucchitta, B. K., Crater clusters and light mantle at the Apollo 17 site-A result of secondary impact from Tycho, *Icarus*, *30*, 80–96, 1977.

Lucey, P. G., G. J. Taylor, and E. Malaret, Abundance and distribution of iron on the Moon, *Science*, *268*, 1150–1153, 1995.

Lucey, P. G., D. T. Blewett, and B. Ray Hawke, Mapping the FeO and TiO_2 content of the lunar surface with multispectral imagery, *J. Geophys. Res.*, *103*, 3679–3699, 1998a.

Lucey, P. G., G. J. Taylor, B. R. Hawke, and P. D. Spudis, FeO and TiO_2 concentrations in the South Pole-Aitken basin: Implications for mantle composition and basin formation, *J. Geophys. Res.*, *103*, 3701–3708, 1998b.

Lucey, P. G., D. T. Blewett, and B. L. Jolliff, Lunar iron and titanium abundance algorithms based on final processing of Clementine ultraviolet-visible images, *J. Geophys. Res.*, *105*, 20,297–20,305, 2000a.

Lucey, P. G., D. T. Blewett, G. J. Taylor, and B. R. Hawke, Imaging of lunar surface maturity, *J. Geophys. Res.*, *105*, 20,377–20,386, 2000b.

Margot, J. L., D. B. Campbell, R. F. Jurgens, and M. A. Slade, The topography of Tycho crater, *J. Geophys. Res.*, *104*, 11,875–11,882, 1999.

Margot, J. L., D. B. Campbell, R. F. Jurgens, and M. A. Slade, Digital elevation models of the Moon from Earth-based interferometry, *IEEE Trans. Geosci. Remote Sens.*, *38*, 1122–1133, 2000.

McEwen, A. S., A precise lunar photometric function (abstract), *Lunar Planet. Sci.*, *XXVII*, 841–842, 1996.

McEwen, A. S., and M. S. Robinson, Mapping of the Moon by Clementine, *Adv. Space Res.*, *19*, 1523–1533, 1997.

McEwen, A. S., M. S. Robinson, E. M. Eliason, P. G. Lucey, T. C. Duxbury, and P. D. Spudis, Clementine observations of the Aristarchus region of the Moon, *Science*, *266*, 1858–1861, 1994.

McEwen, A., E. Eliason, P. Lucey, E. Malaret, C. Pieters, M. Robinson, and T. Sucharski, Summary of radiometric calibration and photometric normalization steps for the Clementine UVVIS images (abstract), *Lunar Planet. Sci.* [CD-ROM], *XXIX*, abstract 1466, 1998.

McGetchin, T. R., M. Settle, and J. W. Head, Radial thickness variation in impact crater ejecta: Implications for lunar basin deposits, *Earth Planet. Sci. Lett.*, *20*, 226–236, 1973.

Meyer, C., *Catalog of Apollo 17 Rocks, Volume 4 — North Massif, JSC 26088*, 644 pp., NASA Johnson Space Center, Houston, Tex., 1994.

Morris, R. V., R. Score, C. Dardano, and G. Heiken, *Handbook of Lunar Soils, Part II, Apollo 16–17, Publ. 67, JSC 19069*, pp. 425–914, NASA Planetary Materials Branch, Johnson Space Center, Houston, Tex., 1983.

Muehlberger, et al., 6, Preliminary geologic investigation of the Apollo 17 landing site, in *Apollo 17 Preliminary Science Report*, *NASA Spec. Publ., NASA SP-300*, 6–1 to 6–91, 1973.

NASA, LUNAR Topographic Orthophotomap, *LTO43D1*, Def. Mapp. Agency Topogr. Cent., Washington, D. C., Oct. 1974.

Neal, C. R., and L. A. Taylor, *Catalog of Apollo 17 Rocks, Volume 2 — Central Valley, Part 1, JSC 26088*, 522 pp., NASA Johnson Space Center, Houston, Tex., 1993a.

Neal, C. R., and L. A. Taylor, *Catalog of Apollo 17 Rocks, Volume 3 — Central Valley, Part 2, JSC 26088*, 522 pp., NASA Johnson Space Center, Houston, Tex., 1993b.

Neukum, G., U. Carsenty, K. Eichentopf, H. Hoffmann, R. Jaumann, J. Oberst, R. Pischel, and G. Schwarz, The experiment HRSC and WAOSS on the Russian Mars 94/96 missions, *Acta Astronaut.*, *38*, 713–720, 1996.

Nozette, S., et al., The Clementine mission to the Moon: Scientific overview, *Science*, *266*, 1835–1839, 1994.

Nozette, S., P. D. Spudis, M. S. Robinson, D. B. J. Bussey, C. Lichtenberg, and R. Bonner, Integration of lunar polar remote-sensing data sets: Evidence for ice at the lunar south pole, *J. Geophys. Res.*, *106*, 23,253–23,266, 2001.

Oberst, J., T. Roatsch, W. Zhang, A. C. Cook, R. Jaumann, T. Duxbury, F. Wewel, R. Uebbing, F. Scholten, and J. Albertz, Photogrammetric analysis of Clementine multi-look angle images obtained near Mare Orientale, *Planet. Space Sci.*, *44*, 1123–1133, 1996.

Oberst, J., M. Waelisch, A. C. Cook, T. Roatsch, and R. Jaumann, Lunar

details gleaned from digital stereo images, *Eos Trans. AGU*, *78*(41), 445, 450, 1997.

Pieters, C., Compositional diversity and stratigraphy of the lunar crust derived from reflectance spectroscopy, in *Remote Geochemical Analysis: Elemental and Mineralogical Composition*, edited by C. M. Pieters and P. A. J. Englert, pp. 309–339, Cambridge Univ. Press, 1993.

Pieters, C., T. B. McCord, M. P. Charette, and J. B. Adams, Lunar surface: Identification of the dark mantling material in the Apollo 17 soil samples, *Science*, *183*, 1191–1194, 1974.

Pieters, C. M., M. I. Staid, E. M. Fischer, S. Tompkins, and G. He, A sharper view of impact craters from Clementine data, *Science*, *266*, 1844–1848, 1994.

Reed, V. S., and E. W. Wolfe, Origin of the Taurus-Littrow massifs, *Proc. Lunar Sci. Conf.*, *6th*, 2443–2461, 1975.

Robinson, M. S., Scattered light in Clementine UVVIS camera, *Lunar Planet. Sci.* [CD-ROM], *XXXII*, abstract 2004, 2001.

Robinson, M. S., A. S. McEwen, E. Eliason, E. M. Lee, E. Malaret, and P. G. Lucey, Clementine UVVIS global mosaic: A new tool for understanding the lunar crust (abstract), *Lunar Planet. Sci.* [CD-ROM], *XXVIII*, abstract 1931, 1999.

Ryder, G., *Catalog of Apollo 17 rocks Volume 1 — Stations 2 and 3 (South Massif), JSC 26088*, 411 pp., NASA Johnson Space Center, Houston, Tex., 1993.

Schmitt, H. H., Apollo 17 report on the valley of Taurus-Littrow, *Science*, *182*, 681–690, 1973.

Schmitt, H. H., and E. A. Cernan, 5, A geological investigation of the Taurus-Littrow valley, in *Apollo 17 Preliminary Science Report*, *NASA Spec. Publ., NASA SP-300*, 5–1 to 5–21, 1973.

Scott, D. H., and M. H. Carr, *Geologic Map of the Taurus-Littrow region of the Moon Apollo 17 Pre-mission Map*, *U.S. Geol. Surv. Map I-800*, scale 1:250,000, 1972.

Spudis, P. D., *The Geology of Multi-Ring Impact Basins, The Moon and Other Planets*, 263 pp., Cambridge Univ. Press, New York, 1993.

Spudis, P. D., and G. Ryder, Apollo 17 impact melts and their relation to the Serenitatis Basin, in *Multiring Basins*, edited by P. H. Schultz and R. B. Merrill, pp. 133–148, Pergamon, N.Y., 1981.

U.S. Geological Survey (USGS), Preliminary topographic map of part of the Littrow region of the Moon, scale 1:50,000, Flagstaff, Ariz., March 1972.

Weitz, C. M., J. W. Head III, and C. M. Pieters, Lunar regional dark mantle deposits: Geologic, multispectral, and modeling studies, *J. Geophys. Res.*, *103*, 22,725–22,759, 1998.

Wilhelms, D. E., *The Geologic History of the Moon*, *U.S. Geol. Surv. Prof. Pap., 1348*, 302 pp., 1987.

Wolfe, E. W., and V. S. Reed, Geology of the massifs at the Apollo 17 landing site, *J. Res. U.S. Geol. Surv*, *4*, 171–180, 1976.

Wolfe, E. W., B. K. Lucchitta, V. S. Reed, G. E. Ulrich, and A. G. Sanchez, Geology of the Taurus-Littrow valley floor, *Proc. Lunar Sci. Conf.*, *6th*, 2463–2482, 1975.

Wolfe, E. W., N. G. Bailey, B. K. Lucchitta, W. R. Muehlberger, D. H. Scott, R. L. Sutton, and H. G. Wilshire, *The Geologic Investigation of the Taurus-Littrow Valley: Apollo 17 Landing Site*, *U.S. Geol. Surv. Prof. Pap., 1080*, 280 pp., 1981.

B. L. Jolliff, Department of Earth and Planetary Sciences, Washington University, Campus 1169, One Brookings Drive, St. Louis, MO 63130, USA.

M. S. Robinson, Department of Geological Sciences, Northwestern University, 1847 Sheridan Road, Evanston, IL 60208, USA. (robinson@earth.northwestern.edu)